ACTINIDE RESEARCH QUARTERLY

Ac Th Pa U Np Pu Am Cm Bk Cf Es Fm Md No Lr

Second Quarter 2022

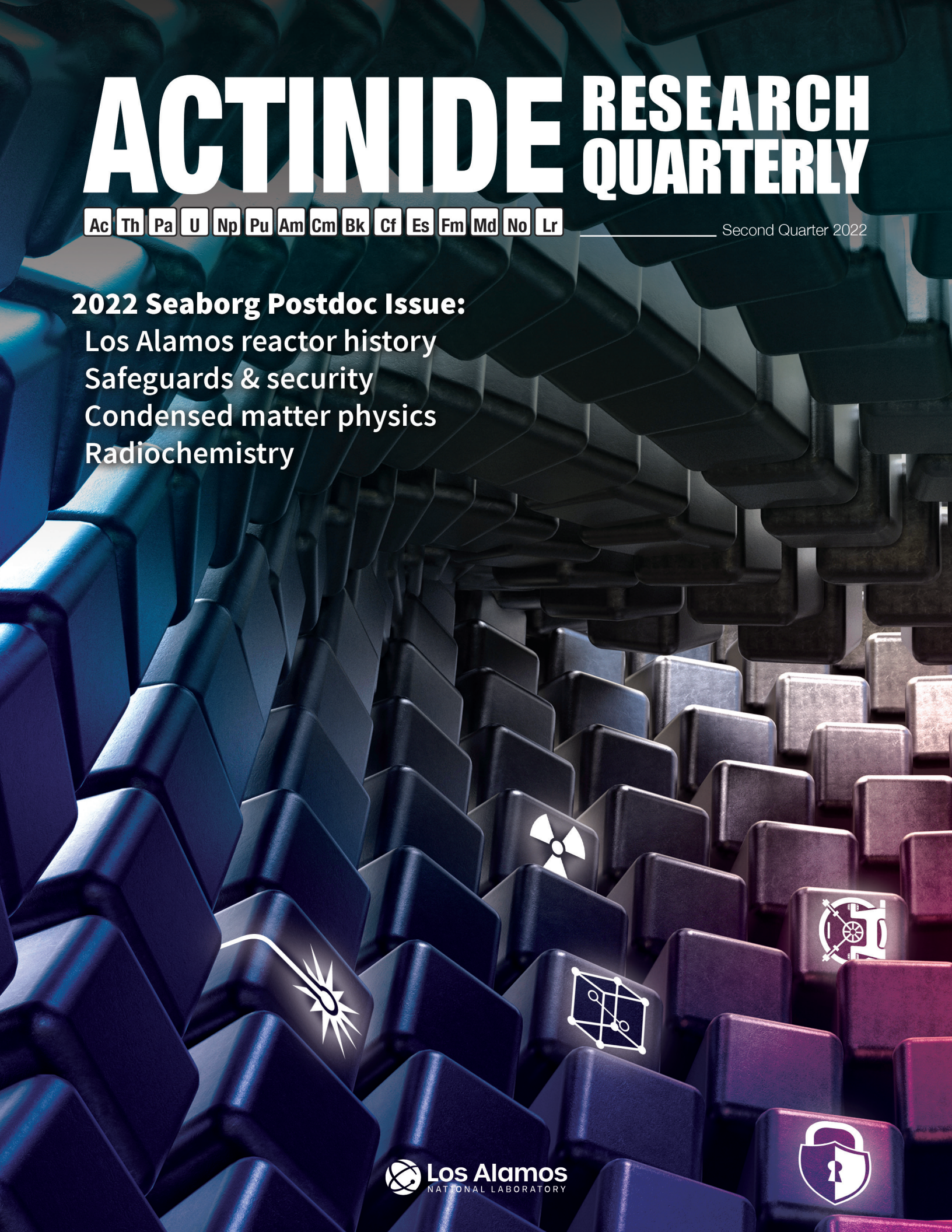

2022 Seaborg Postdoc Issue:

Los Alamos reactor history
Safeguards & security
Condensed matter physics
Radiochemistry

Los Alamos
NATIONAL LABORATORY

Foreword

In this issue, we present our annual collection of articles contributed from Los Alamos Seaborg Institute graduate and postdoctoral researchers. Through the program, the Seaborg Institute aims to advance actinide science, technology, and engineering relevant to Los Alamos missions and to provide an entry point for exceptionally qualified potential employees.

The Los Alamos Clementine reactor was the world's first fast nuclear reactor. It generated an enormous quantity of nuclear data, informed future reactor designs, and yielded the first aging studies of delta-phase plutonium. In her graduate work at Los Alamos this summer, Hannah Patenaude has subjected the historical Clementine data to a modern computational analysis, incorporating engineering details of the design. As an aspect of this work, she has written a carefully researched history article, which we present here (p2).

In the world of nuclear forensics and nonproliferation, there is a need to develop additional signatures and new methods to constrain baseline forensic analysis. Arjen van Veelen's article on p10 presents a novel microprobe that can identify particles with subtle molecular variations relevant to nuclear forensic science. His work focuses on uranium oxide, the most common form of illicitly trafficked special nuclear material.

We have two articles on the subject of materials science and condensed matter physics. In "Uranium Dioxide Sings to the Beat of a Magnetic Hammer," Rico Schönemann describes magnetostriction studies (i.e., changes in sample length) at high magnetic field and low temperatures (p18). Previous work at the National High Magnetic Field Laboratory in Los Alamos has shown uranium dioxide to be the strongest known piezomagnet. In Schönemann's work, the extremely large rate-of-change of the applied magnetic field is equivalent to hitting the uranium dioxide crystal with a "magnetic hammer," exciting a "song" composed of mechanical resonances in the range of several hundred kilohertz. Yogesh Sharma also uses uranium dioxide in his studies (p24) to examine the possibility of using epitaxial strain to tailor the physical properties of thin films, using the actinide thin film capability established at Los Alamos National Laboratory. He shows that it is possible to engineer ferromagnetism in uranium dioxide with lattice strain and produce a magnetically-uniform insulating thin film that could be used for next-generation magnetic devices.

The highly radioactive and short-lived isotope actinium-225 has shown promise for targeting and attacking certain types of cancer cells. Although no treatment using the actinide has yet been approved by the FDA, the US Department of Energy Isotope Program has identified actinium-225 as a critical isotope because of its high demand and limited availability. Since 2014, the program has sponsored a Tri-Lab research effort involving Brookhaven, Los Alamos, and Oak Ridge National Laboratories to provide accelerator-produced actinium-225 for radiotherapy. On p29, Kelly Aldrich describes her work establishing a generator procedure for the less hazardous and more spectroscopically friendly actinium-228 isotope to be used in synthetic studies that support the development of actinium-based therapeutics.

— Owen Summerscales, Editor

About the cover: The Glenn T. Seaborg Institute supports a wide range of research in actinide science and technology. In this issue we present the Seaborg Institute-funded work of several postdoctoral researchers at Los Alamos, covering the diverse subject areas of condensed matter physics, Los Alamos reactor history, safeguards and security, and radiochemistry. The cover attempts to signify these different research areas.

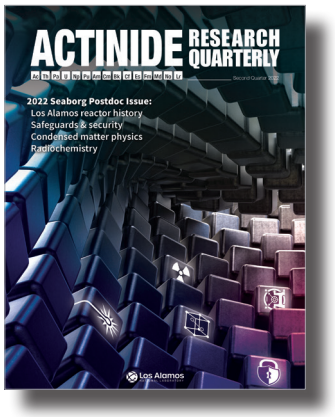

Contents

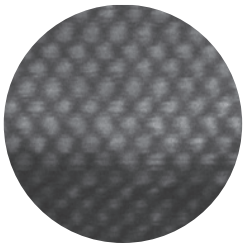

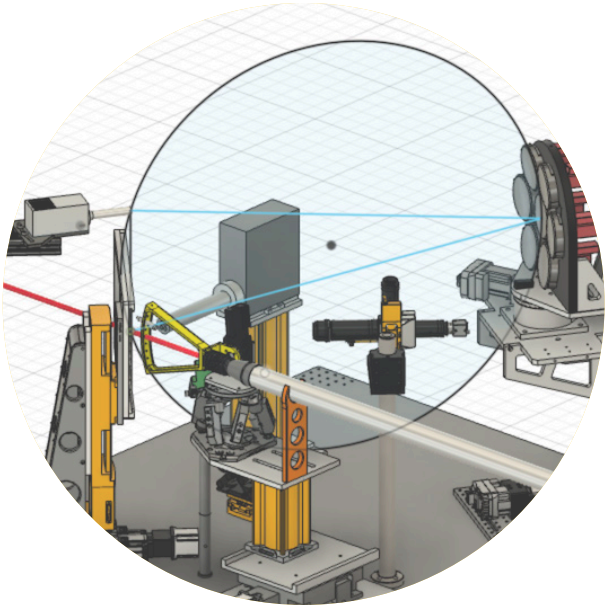

Hannah Patenaude

Hannah Patenaude was a Seaborg Graduate Research Assistant for the summer of 2022 studying the Clementine Reactor under mentor Franz Freibert. She is currently a PhD student at the University of Nevada, Las Vegas in the Radiochemistry Program. Her dissertation research focuses on actinide molten salt electrochemistry.

Oh, My Darling Clementine: A History of the Los Alamos Plutonium Fast Reactor

Hannah K. Patenaude, Franz J. Freibert
Los Alamos National Laboratory, Los Alamos, New Mexico 87545

In a cavern, in a canyon
Excavating for a mine
Dwelt a miner forty-niner
And his daughter, Clementine

One 'miner,' physicist Philip Morrison, brought to life the world's first fast nuclear reactor, his daughter Clementine. She was constructed on the side of a Los Alamos canyon in the immediate aftermath of World War II and christened by Morrison after the hit gold rush folk song, "Oh My Darling, Clementine." It was a particularly fitting theme given its location near the Water Boiler reactor at the Omega Laboratory (TA-2), which required moderate excavation into the canyon wall. Additionally, because the code for plutonium-239 in written correspondence was the combination of its atomic number (94) and mass number (239), '49,' team members on this project were aptly referred to as 'miner forty-niners.'

Also called the Los Alamos Plutonium Fast Reactor , Clementine "was to be different in principle from all other existing reactors," and supported the need for high-intensity, high-energy neutrons towards weapons development. The project simultaneously investigated the prospect of using fast neutrons and breeding fissile material for commercial power production. Since then, no reactor has been cooled by mercury, given the development of other heavy metals such as lead and alloys like sodium-potassium. Additionally, metallic fuels have steered away from plutonium-gallium and toward ternary eutectics such as U-Pu-Zr. However, Clementine provided a wealth of fundamental data that paved the way for modern and advanced reactor technology in a variety of areas within the nuclear energy industry. Specifically, Clementine influenced the design of the Omega West reactor, which both physically and technologically replaced the fast reactor. The data also informed work at the Experimental Breeder Reactor I (EBR-I), which carried the torch across the finish line in 1953 to produce fissile material in situ. Finally, the results gave both a foundation for liquid fast reactors cooled by liquid heavy metals and a strong proof-of-concept for fast neutron spectrum reactors.

An early timeline of Clementine

When Enrico Fermi moved to Los Alamos from the Chicago Metallurgical Laboratory—where progress on EBR-I was being quickly made—he carried with him an interest in pursuing a breeder reactor design, ultimately inspiring Morrison's concept for Clementine (Morrison previously worked for Fermi in Chicago). It was intended to operate at low power (10–25 kW) and serve as an experimental fast neutron facility that could also demonstrate plutonium's use as a fuel.

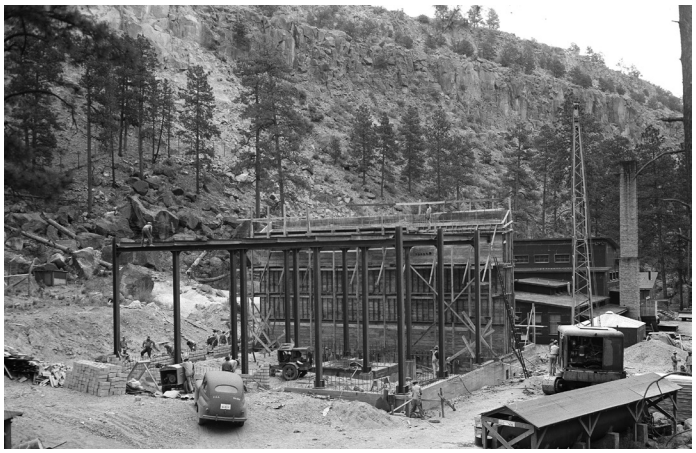

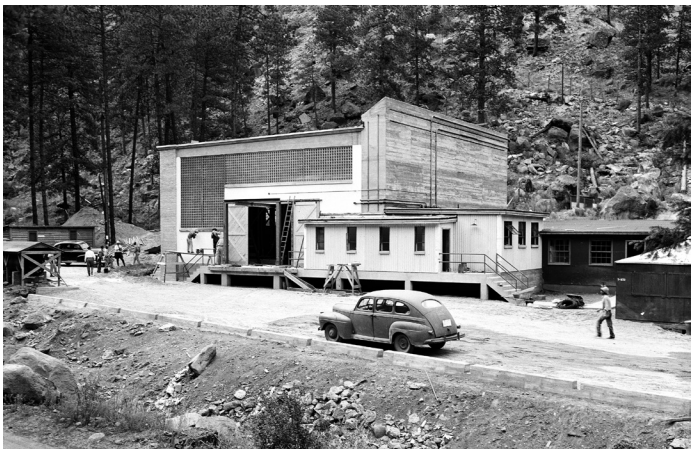

Figure 1. Construction of the new Clementine building next to the Omega Laboratory at the TA-2 site, nestled within Los Alamos Canyon.

o o o

Records were well kept in the many letters sent between Manhattan Project participants around the country regarding the development of the fast reactor. The first written discussion relevant to Clementine came at the end of 1944, when Bernard Feld wrote to Leo Szilard about the results from an investigation into fast neutron energy distributions. The following year came with more specific correspondence between Percible King and John Manley, outlining ways to plan construction around the existing Water Boiler reactor and any new critical experiments coming to Omega Site in the canyon.

By the fall of 1945, Morrison, George Placzek, and Louis Slotin began considering the possibility of redirecting those critical experiments toward the development of a device capable of generating a fast neutron spectrum. By November 10, a team of experts was assembled for the first of four 'Power Reactor Notes' meetings for preliminary discussions and planning for the development of Clementine. Less than two weeks later, on November 23, 1945, Los Alamos Director Norris Bradbury wrote to Lieutenant General Leslie Groves, officially requesting a non-weapons grade quantity of plutonium to construct a fast reactor. Approval came in extraordinary speed from Washington, D.C. on December 17.

Vigorous planning began in early January, 1946, including requests for uranium from Madison Square Area* and thorium from Iowa State College. Communication and collaboration with Wally Zinn's EBR-I team at Chicago was strengthened, and designs for fabricating the plutonium fuel slugs were in full swing by the end of the month. Mercury circulation pumps were deliberated in March. By the end of May, a letter to Morrison from his team described many technical specifications in great detail, including tamper material, safety and control devices, sample and experimental holes, tamper cooling, shielding, slug information, reactor instrumentation, beta and gamma measurements, mercury vapor detection, nuclear measurements leak detection, and mass estimations.

This pace was maintained over the summer. By the fall of 1946, Clementine was adopted by husband-and-wife team David and Jane Hall when Morrison accepted a

* Madison Square Area in New York, NY served as a central office for record-keeping and classified correspondence during the Manhattan Project from 1942–1947.

position at Cornell University, but close correspondences and visits continued with Morrison. On September 12, Darol Froman sent Lieutenant C. O'Brien a finalized list of individuals who were cleared to receive active material (plutonium) from the security guard, namely: Morrison, the Halls, King, and Jerome Kellogg. The "dream team" had been fully assembled, and next up would be the plutonium. When the team assembled the active material, Clementine was brought to life. She operated only for three days, however, before a tamper malfunction required disassembly that lasted for approximately two months. In their downtime, the team produced a list of planned experiments. Irradiation testing was orchestrated through the Hanford site with the manufactured plutonium slugs because the flux at the Water Boiler next door was not high enough. The critical assembly of Clementine was reconstructed on November 21, and some preliminary results were sent from the Halls to Morrison in December.

An entire reactor had been built and assembled within a single year—clearly, an unimaginable amount of work was accomplished in an incredibly short amount of time. More than 20 years after her disassembly, Norris Bradbury reflected on his tenure as Director of the Laboratory throughout Clementine's lifetime:

> *We made the first plutonium reactor, called Clementine, and it was the first reactor that operated upon a fast neutron spectrum. I only pause to note that today it would take you ten billion dollars and fifty thousand volumes of environmental reports and nobody'd let you do it anyway, but we just did it. And it worked beautifully; we finally shut it down when it became clear that some of the components were a little tired.*
>
> — N. Bradbury, *Reminiscences of Los Alamos 1943–45*, 1980.

Initial operation and experimentation

According to a letter from the Halls updating Morrison, critical assembly measurements began November 19, 1946, and the experiments warranted a biblical reference: "We concluded from our estimates of control rod effect which were based on multiplication measurements on the way up to critical, that about 23.6 slugs were critical. (Obviously demanding the sixth verse of the Twenty-third Psalm.)."

Low power measurements were conducted until February, 1947, then the power was increased to 10 kW for twenty-one months while the core was still being referred to as a 'critical assembly,' during which they determined factors such as critical mass versus core configuration, effectiveness of reactor control, reactor temperature coefficient, effect of temperature and reactivity changes in reactor operations, and neutron energy distribution in the center of the reactor. Additionally, the team employed the Danger Coefficient Method of introducing various materials into the core to monitor reactivity changes, thus providing novel insight into the neutron cross-sections of over forty isotopes. The term "danger coefficient" was likely a result of the growing concern over criticality accidents, two of which had occurred in recent years in Morrison's group.[†]

It was not until January of 1949 that the final assembly was complete, and Clementine came to full power in March. She operated for a year before issues arose with function of the control and safety rods, resulting in the first of two failures that occurred throughout the fast reactor's lifetime. The reactor was shut down and opened for investigation in May, 1950.

† Harry Daghlian and Louis Slotin were both killed at Los Alamos by supercritical events (in 1945 and 1946, respectively) as a result of accidents with a subcritical core of plutonium, often referred to as the "demon core."

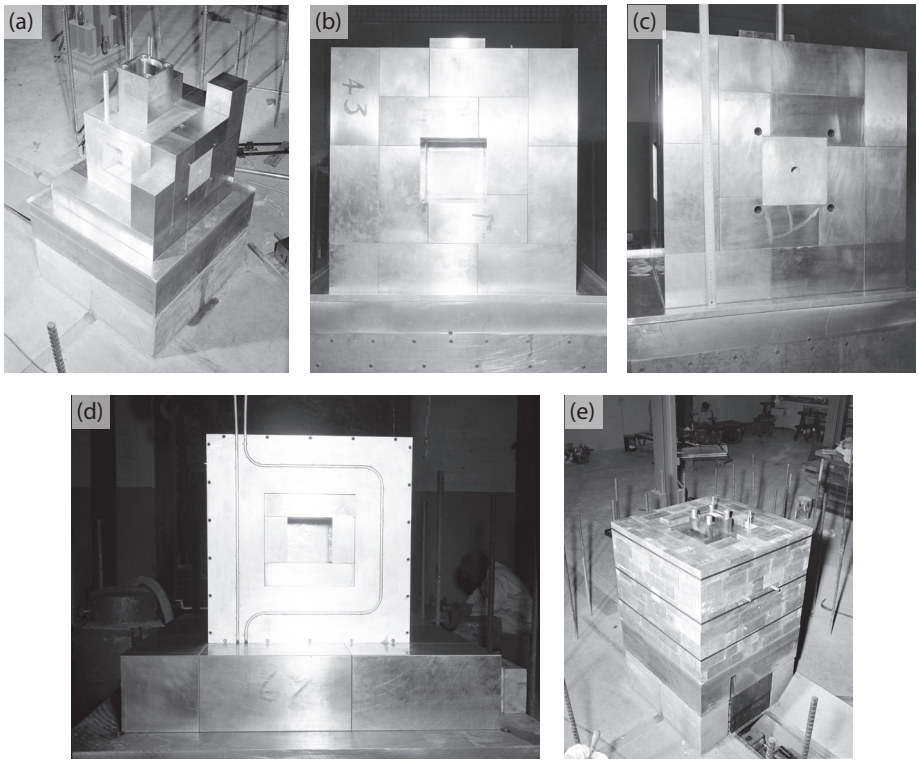

Figure 2. (a) Partially constructed uranium tamper showing the locations for the thorium window (*left*) and uranium window (*right*). (b) Thorium window and (c) uranium window within the uranium tamper cube. The face with the uranium window shows a set of experimental holes used to access the active region. (d) Aluminum jacket for tamper water cooling system that removed heat generated by the uranium blocks (*right*). (e) Lead bricks surrounding the tamper.

Figure 3. Complete structure of the Clementine reactor with stair access to the pile. Inset: Commemorative plaque on the stairs leading to the pile.

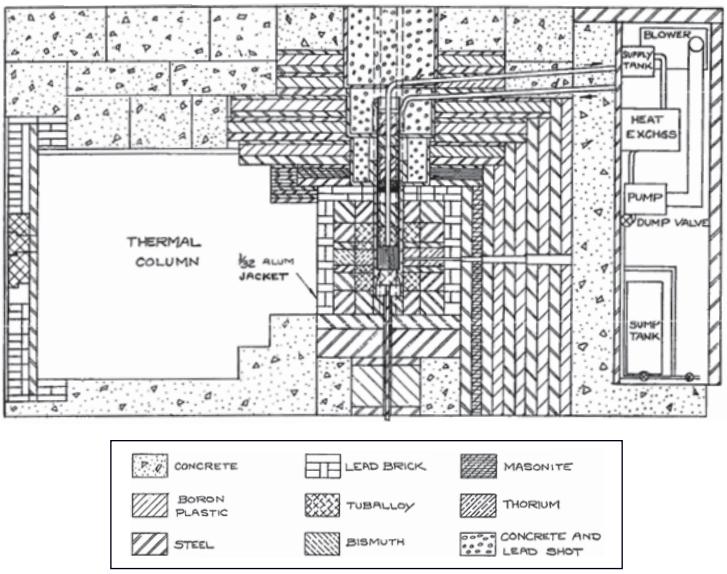

Figure 4. Schematic cross-section of Clementine.

Failure 1: Wedged slugs

After exploring the impacts of temperature and reactivity on the operation of the reactor, it was concluded in 1948 that blistering of the safety block and rods was "not expected to cause trouble during the reactor's life-time." Yet, this was, in fact, the first failure experienced by Clementine. After approximately one year of operation, it was estimated that the fuel rods were thermally cycled between 500 and 800 times from 25 to 150°C. For 450 g plutonium slugs, it was estimated that approximately 7.5×10^{19} fissions had occurred in this time, and 1.4×10^{19} for 580 g uranium slugs (4% due to uranium-235).

When the control and safety rods became frozen in their channels in March 1950, the reactor was shut down for examination. It was discovered that two of the uranium slugs were wedged in the cage along with one of the plutonium fuel slugs. Of the two uranium rods, #141 showed a significant crack in the steel jacket along with several surface blisters (Fig. 5a), and #205 had a single blister on the surface of the jacket. They were taken for further inspection and were not returned to the reactor.

The wedged plutonium slug was not identified numerically, other than its location being adjacent to uranium slug #141, but reportedly suffered no visible damage. However, X-ray radiography performed on the plutonium rods while the core was disassembled exposed an interesting phenomenon that warranted further analysis. It appeared as though gaps were present between the uranium wafer and plutonium rod that were not observed in 1947 before irradiation in the pile.‡ The change in total gap spacing around the plutonium slug was recorded based on X-ray imaging and compared to information recorded before reactor operation. The height of the uranium wafer was unchanged, and it was concluded that the original density of plutonium correlated with the observed shrinkage of the active material. This change was thought due to the dimensional destabilization of the δ-phase plutonium, transitioning to a higher-density phase from heat cycling and/or irradiation.

‡ Uranium wafers were inserted below the plutonium alloy fuel rod within the steel can to protect the plutonium from reaction during welding operation as the fuel was fabricated.

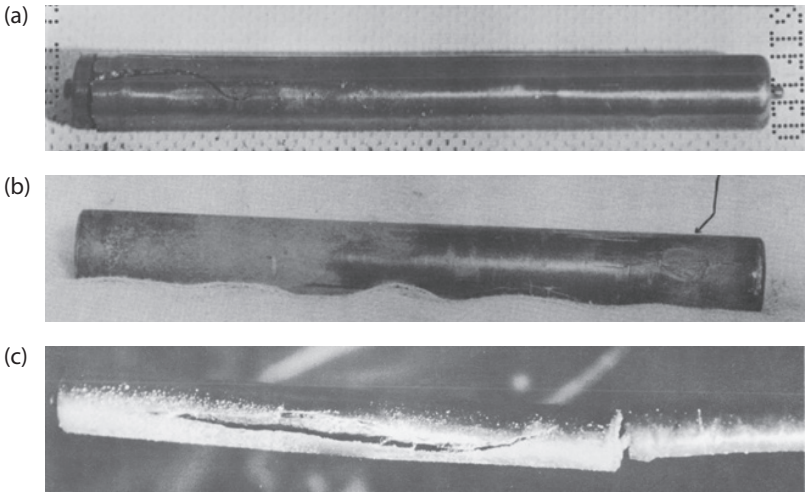

Figure 5. (a) Cracked steel can for uranium rod #141 removed after the first failure. (b) Irradiated plutonium rod #66 laying on a bed of cheese cloth with shriveled spot and crack located under the arrow. (c) Ruptured plutonium fuel rod responsible for Clementine's second failure.

o o o

A seemingly undamaged fuel rod was chosen to examine for any other evidence of evolution in the material. Although the steel jacket was unchanged and not distorted, there were three longitudinal cracks found in the nickel coating of the plutonium-gallium rod. The cladding was removed and uncovered many small cracks in the plutonium, itself. Additionally, there was one large round spot that was described as "shriveled and cracked" (Fig. 5b).

The core was slightly reconfigured in order to resume operation. A new basket with fewer holes (37 instead of 55) was fabricated. In this case, only 32 of the holes would contain plutonium slugs and the five remaining would be filled with steel cans, each with a small hole in the bottom and top so the mercury could flow slowly through minimizing disruption of the coolant flow pattern within the cage. Again, each of the plutonium rods were radiographed, cleaned, and tested for leaks with a mass spectrometer leak detector before reassembly.

This new critical assembly was completed on June 27, 1950, and welded closed two days later. A power level of 25 kW was resumed on July 17, with the temperature of the central plutonium slug measured at 170°C, compared to 155°C from the original loading. However, this was expected considering there are 32 instead of 35 fuel slugs, therefore the heat exposure per slug has increased. Additionally, a slight increase in reactivity was reported, as would have been suggested from previously noted nuclear reactivity changes, but Jane and David Hall believed that it fell well within their control limits and "no hazard appears to exist."

Failure 2: Alpha-contaminated coolant

Clementine operated for nearly two more years before the second failure occurred. By the second half of 1952, there were two apparent issues that would become problematic in future operation: the safety block was sticking and failing to seat, and the control rods were binding in their operating passageways. They concluded that both problems were a result of fission product build-up and warpage due to abnormal crystalline growth of the uranium blanket, including the safety block. However, this was not the failure that concluded Clementine's operation.

For the last two years of operation, regular monitoring for alpha contamination was conducted in samples of the mercury coolant in order to detect any ruptures of plutonium fuel rods. Unfortunately, on Christmas Eve of 1952, considerable quantities of alpha activity were found in the mercury and operation of the reactor was immediately stopped for the final time. Disassembly began soon after.

Disassembly

The disassembly of Clementine was no trivial task. The mercury coolant was now heavily contaminated with alpha radiation in the form of plutonium. Additionally, they calculated the gamma radiation from each of the 32 fuel rods would be 10–20 Ci. It was necessary to conduct disassembly procedures under an inert, dry atmosphere in order to prevent contamination of surfaces in the room that housed Clementine. To reduce radiation exposure for the workers, remote-control handling was required for certain operations.

Disassembly was to be completed in a specific sequence of steps: (1) removal of mercury coolant, (2) cutting of mercury coolant pipes, and (3) removal of fuel rods and "top tamper" assembly that filled the pot above the assembly. Step (1) required two separate operations: first, draining of the supply tank, pump, heat exchangers, and plumbing into the mercury cabinet through the petcock which was installed for that purpose. Second, the coolant trapped in the pot and any connected pipes would have to be removed in conjunction with steps (2) and (3). All containers required appropriate shielding for radiation purposes, in addition to proper sealants to prevent the loss of plutonium into the environment.

Two of the fuel rods were especially difficult to remove, not coming loose even with hard, two-handed pulling. It eventually became necessary for the team to saw sections off the top plate of the cage. Although one of the stuck rods showed no visible damage, the other was badly ruptured and was clearly the source of plutonium contamination into the coolant system (Fig. 5c).

Figure 6. Removing the remainder of the tamper required the welding of two 4″ I-beams to the supporting plate below the tamper unit. The beams were welded onto skids made of larger I-beams so the assembly could slide across the floor and onto the adjacent loading dock, where it was loaded onto a truck for transportation to the South Mesa contaminated area and covered with a wooden shack for protection against the weather.

Figure 7. *Left*: Philip Morrison, father of the Clementine design, in 1945. *Right*: Jane and David Hall, adopted parents of Clementine, the Los Alamos Plutonium Fast Reactor.

Summary

Clementine, the Los Alamos Plutonium Fast Reactor, was one of the most radical and rapidly developed reactors ever built. She created the foundation upon which the nuclear energy industry still operates today, and the surplus of data that came from those few short years has proven invaluable. This data included key characteristics of dozens of material nuclear cross-sections, which furthered the understanding of reactor design and performance and pushed innovation in the area of reactor safety and decommissioning. The accomplishments of Clementine span multiple subfields within the nuclear industry, and in particular form a proof-of-concept for fast spectrum neutron reactors, metal-fueled designs, and those with metal-coolant systems. Additionally, Clementine served as Louis Rosen's first experimental neutron source, 10 years before he established the Los Alamos Meson Physics Facility which developed into today's Los Alamos Neutron Science Center (LANSCE). This work supported the advancement of neutron diagnostics to be employed in later bomb development tests.

Now that the industry is well past the days of danger coefficients, many consider Clementine's operation as merely a small point along the timeline of nuclear technology development. However, pioneers like Philip Morrison, Jane Hall, and David Hall walked so we could sprint toward solutions for global threats such as nuclear security and climate change. Although lost and gone forever, as the song goes, there is no dreadful sorrow for Clementine given all that she provided from the peak of the Atomic Age through today. She lives on through the archives of national laboratories, technical summaries and retrospectives, and the designs of advanced reactors being constructed today.

Further reading:

1. *H.K. Patenaude, F.J. Freibert; "Oh, My Darling Clementine: A Detailed History and Data Repository of the Los Alamos Plutonium Fast Reactor" submitted for publication in Nuclear Technology, 2022.*
2. *J.H. Hall, "Plutonium Fast Reactor at Los Alamos," LAMS-567, 1947.*
3. *J.H. Hall, "Fast Plutonium Reactor Experimental Facilities," LAMS-908, 1949.*
4. *J.H. Hall, "Modification of the Los Alamos Fast Plutonium Reactor," LA-1163, 1950.*
10. *E.T. Jurney, D.B. Hall, J.H. Hall, "The Los Alamos Fast Plutonium Reactor," LA-1679, 1954.*

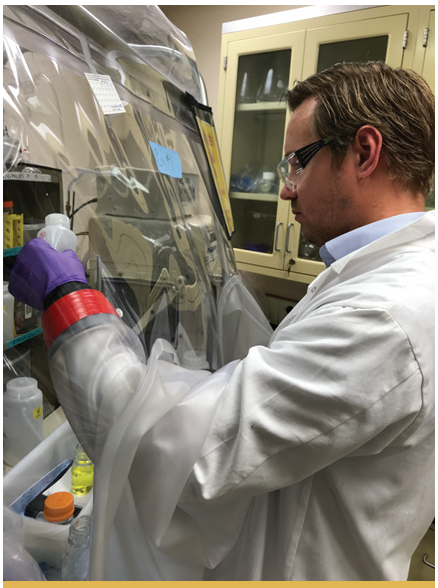

Arjen van Veelen

Arjen van Veelen joined LANL in 2019 as a Seaborg Postdoctoral Researcher under the mentorship of Alison L. Pugmire (MST-16) and John R. Bargar (Stanford Synchrotron Radiation Lightsource, currently at Pacific Northwest National Laboratory). He became staff member in January 2022 (MST-8). Dr. van Veelen received his Ph.D. in Geochemistry in 2014 from the University of Manchester, UK. Before joining LANL, he was a postdoctoral research associate at the University of Manchester and a Research Fellow at the University of Southampton. Dr. van Veelen is an expert in multiple techniques of synchrotron X-ray spectroscopy and imaging, data acquisition, fitting and interpretation. He is currently involved in multiple projects, such as nuclear forensic studies and novel fuel characterization for which he is using advanced spectroscopy methods.

High Energy Resolution Fluorescence Detection: A Probe for Nuclear Forensic Science

Arjen van Veelen
Los Alamos National Laboratory, Los Alamos, New Mexico 87545

Proliferation of nuclear materials and classified information poses grave threats to national security. This can include nuclear weapons program knowledge as well as the potential for theft and diversion of uranium feedstocks and special nuclear materials (SNMs, i.e., enriched uranium and plutonium). Uranium oxides, principally UO_2, are widely used as fuel in reactors and are the most common form of illicitly trafficked SNM. It is therefore crucial to develop nuclear forensic signatures and methods that can determine points of origin, synthesis processes and storage conditions, and intent to do harm. While baseline nuclear forensic methods (e.g., inductively coupled plasma, ICP, secondary-ion mass spectrometry, SIMS, and scanning electron microscopy, SEM) are effective in many cases, analysis of recovered material is still often incomplete, such as with micro-particles, which present challenges of small sample size, heterogeneity, and the presence of multiple phases. Moreover, if the processing history for the parent material is unknown, or if characteristics are not retrievable from nuclear databases, then baseline methods (phase identification, impurity quantification, and isotope analysis) will be less conclusive. Therefore, there is an ongoing and urgent need for additional signatures and new methods to further constrain forensic analysis. Molecular signatures (i.e., molecular structures of trace impurity metals and dopants, their oxidation states, and host phase structural defects) encode nuanced information about individual chemical processing steps used during synthesis, independent of feedstock origin or final product.

Stoichiometric technological UO_2 corrodes over time to U(VI) oxyhydroxide (e.g., meta-schoepite minerals) at low temperatures or to U_3O_8 at high temperatures. Crucially, the intermediate alteration products—UO_{2+x} (x = 0–0.25) and more oxidized products—have unique molecular signatures that can be detected using X-ray absorption spectroscopy (XAS). In contrast, molecular signatures cannot be extracted from traditional mass spectroscopy-based forensic techniques, which provide primarily compositional information (including nuclear mass), are slow (requiring weeks of preparation), and are destructive to samples. Moreover, while X-ray diffraction (XRD) can quantify unit cell contraction upon UO_2 oxidation in pure bulk materials, it is very difficult to use XRD to detect and quantify unit cell changes in small particles (nano- to micro-scale) embedded in complex materials such as soils, which is an important category of forensic samples. Although uraninite oxidation has been the focus of much research over the years, there remain important gaps in our knowledge of the reaction pathway and process rates under environmental conditions. These gaps are particularly significant in the context of forensic analyses, where alteration pathways and kinetics accuracy are critical.

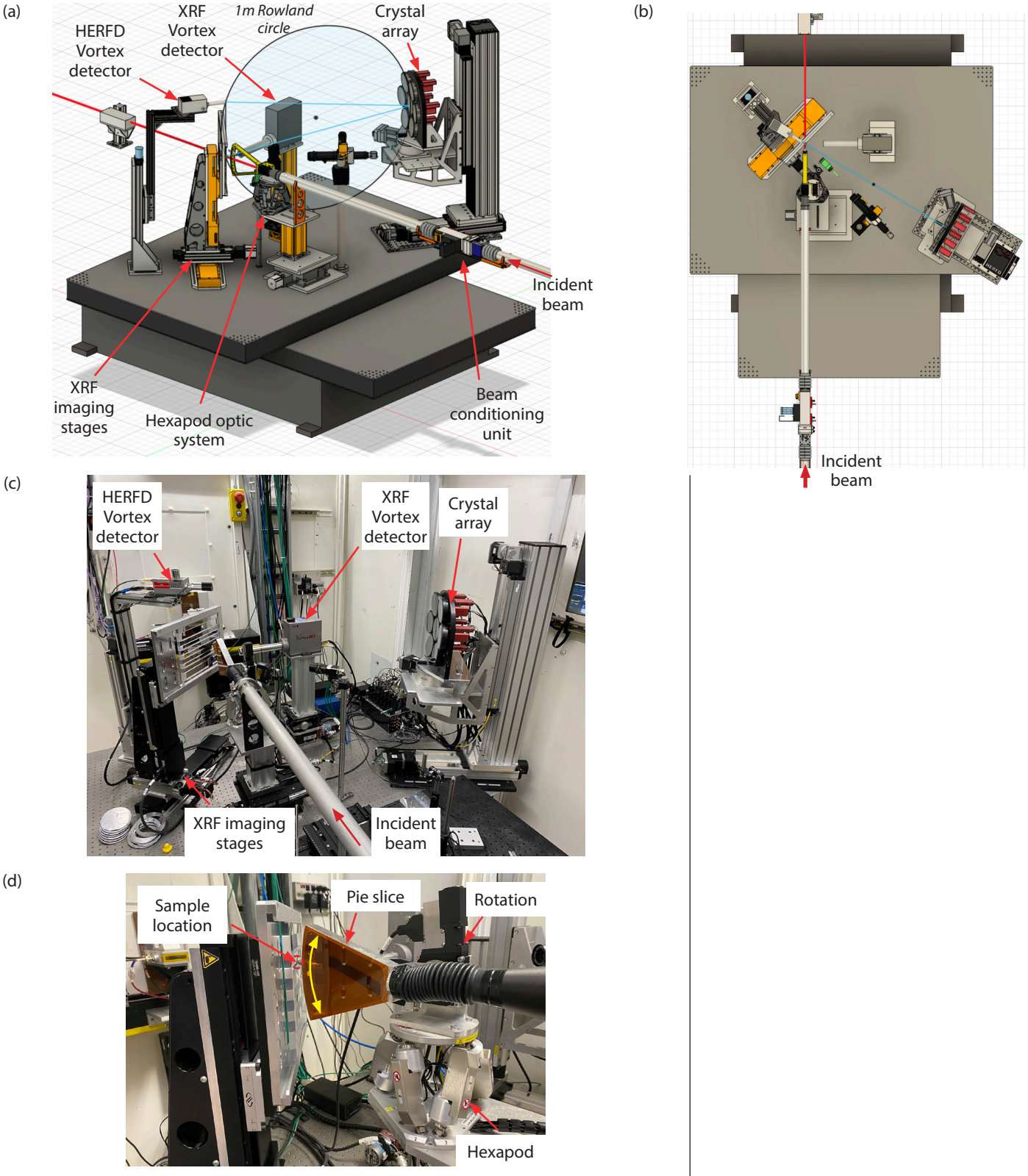

Figure 1. Beamline 6-2 high-energy resolution fluorescence detection (HERFD) imaging spectrometer. (a,b) CAD models of the HERFD instrument installed. (c) Photograph of instrument with a comparable viewpoint as panel (a). (d) Closer view of the rapid aperture/optic changing system. Credit: Nicholas P. Edwards. This figure has been taken from Edwards et al., (2022), "A new μ-high energy resolution fluorescence detection microprobe imaging spectrometer at the Stanford Synchrotron Radiation Lightsource beamline 6-2."

Spectral signatures (absorption peaks and intensities) found in the synchrotron-based extended X-ray absorption spectroscopy fine structure (EXAFS) region and high-energy resolution fluorescence detection X-ray absorption near-edge structure (HERFD-XANES) are extremely sensitive to local and intermediate range structure and composition. XANES spectra can be collected more quickly and from more dilute samples, and thus are a technique of choice for forensic analysis, particularly in imaging mode. However, conventional absorption-mode XANES spectra often lack sufficient spectral fingerprints to distinguish between different coordination chemistries of uranium and plutonium. *The dramatically enhanced energy resolution of HERFD-XANES allows it to detect such structural differences*, and therefore it could be very useful in forensic applications.

We aim to achieve rapid and nondestructive detection of forensic samples as small as micro-particles and determine whether these samples are naturally-occurring or illicit in origin. To that end, we performed state-of-the-art bulk EXAFS and HERFD-XANES analyses to benchmark molecular signatures. This enabled us to develop and identify subtle variations between different UO_{2+x} particles and in complex matrices to better understand the impacts of slight alterations on the molecular and spectral signatures. This formed the foundation for developing a high-energy resolution fluorescence detection (HERFD) microprobe that allowed us to integrate high sensitivity elemental information (parts-per-million level) with molecular information at the micrometer scale, further enhancing our analytical capabilities.

Structural signatures of UO_2 and UO_{2+x}

To establish molecular signatures for determining the storage and processing histories of interdicted uranium oxides (uraninite), it is necessary to understand the processes of molecular transformations that occur at air-oxide interfaces—and their rates—under relevant environmental conditions (e.g., variable humidity, temperature). UO_2 exhibits a rich structural chemistry, derived from its open fluorite structure. Half of the cubically-coordinated interstitial sites in the unit cell are vacant and serve as conduits and resting sites for excess oxygen atoms. These transformations generally involve rearrangements of neighboring oxygen and uranium atoms in the local- and intermediate-range molecular environment around individual uranium atoms (Fig. 2). Beyond U_4O_9, the overall fluorite crystal structure transforms into another configuration, such as U_3O_8 (above ~800°C) or schoepite-like structures (at ambient temperatures). Both transformations break the cubic symmetry and are diagnostic of formation conditions.

Bulk EXAFS and HERFD-XANES: Determination of molecular signatures

To create a fundamental molecular basis for interpreting HERFD-XANES spectra, a detailed understanding of the molecular structure is needed. For this, we synthesized UO_2 and UO_{2+x} via thermogravimetric analysis and subsequently performed measurements using bulk EXAFS (Fig. 3). The effects of increasing x in UO_{2+x} show a gradual decrease in the intensities of the amplitudes in both the EXAFS and Fourier transform. Interestingly, the small increase of oxidation has a huge impact on the local ordering of UO_2. The results prove that our synthesis was successful because no indications of other phases were observed, as these would induce changes in the U-U pair correlation distances. More importantly, these results also demonstrated that EXAFS is indeed a sensitive method for probing minute changes in the oxidation state and local structure of UO_2. Furthermore, this data will serve as a future database for benchmarking x in UO_{2+x}.

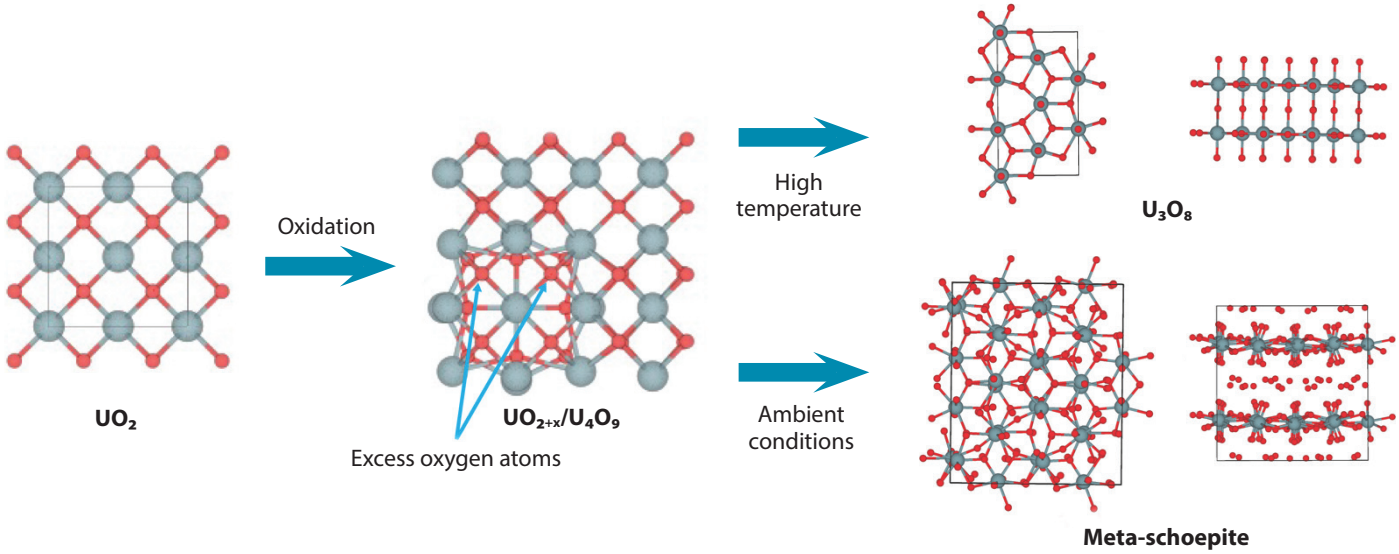

Figure 2. Structural transformation of stoichiometric UO_2 → UO_{2+x} / U_4O_9 ($UO_{2.25}$). Oxidation will induce local re-arrangement of oxygen atoms that will eventually coordinate in localized clusters of higher oxidation state uranium oxides, also called defect clusters. In these, the oxygen atoms are arranged into a cuboctahedron configuration while keeping the overall fluorite structure for UO_2. Beyond $UO_{2.25}$, the crystal structure transforms and will form U_3O_8 (elevated temperatures) and/or meta-schoepite (ambient conditions).

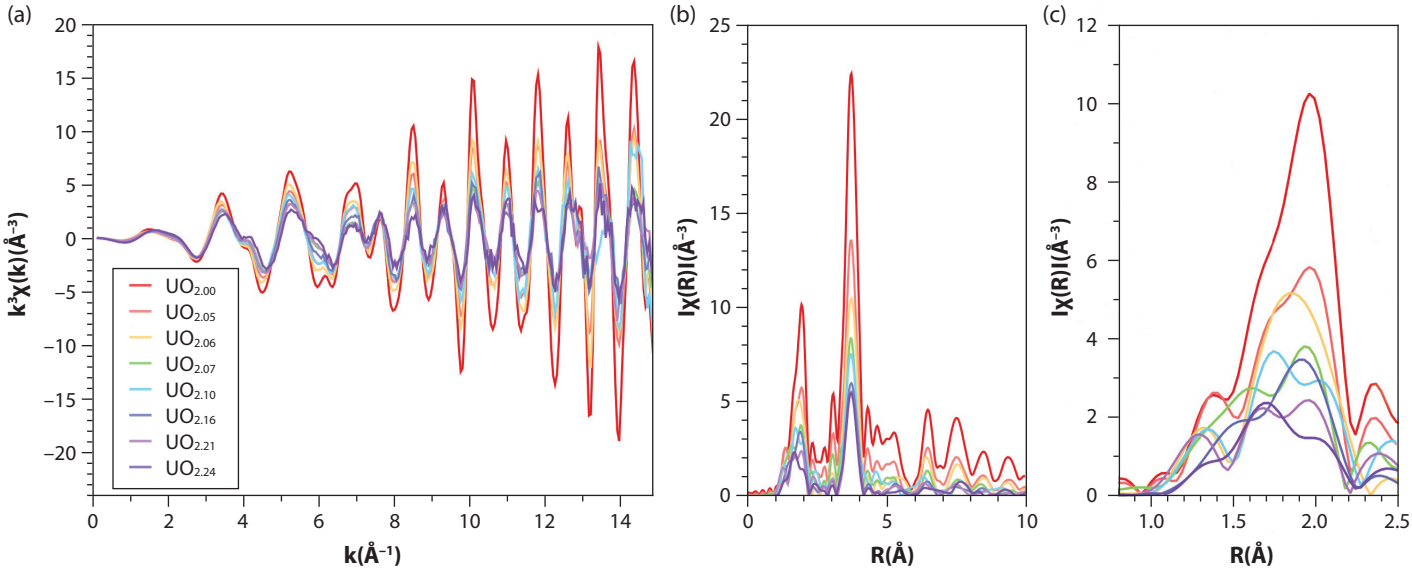

Figure 3. Extended X-ray absorption spectroscopy fine structure (EXAFS) data for the UO_{2+x} series: (a) Full EXAFS of the UO_{2+x} series. Note the dramatic change in amplitude of the oscillations. The amplitude is decreasing with increasing *x*, as shown in (b) The Fourier transform of the data. Note the dramatic decrease in the peak intensities and the shift in U-O pair correlation at ca. 1.9 Å (uncorrected for phase shift as per convention). (c) Expanded region of the O peaks at ca. 1.9 Å, which shows the shift in the U-O pair correlation more clearly. This means that the local molecular structure around U atoms is changing and that the O atoms are re-arranging to shorter distances to ultimately form cuboctahedron configurations.

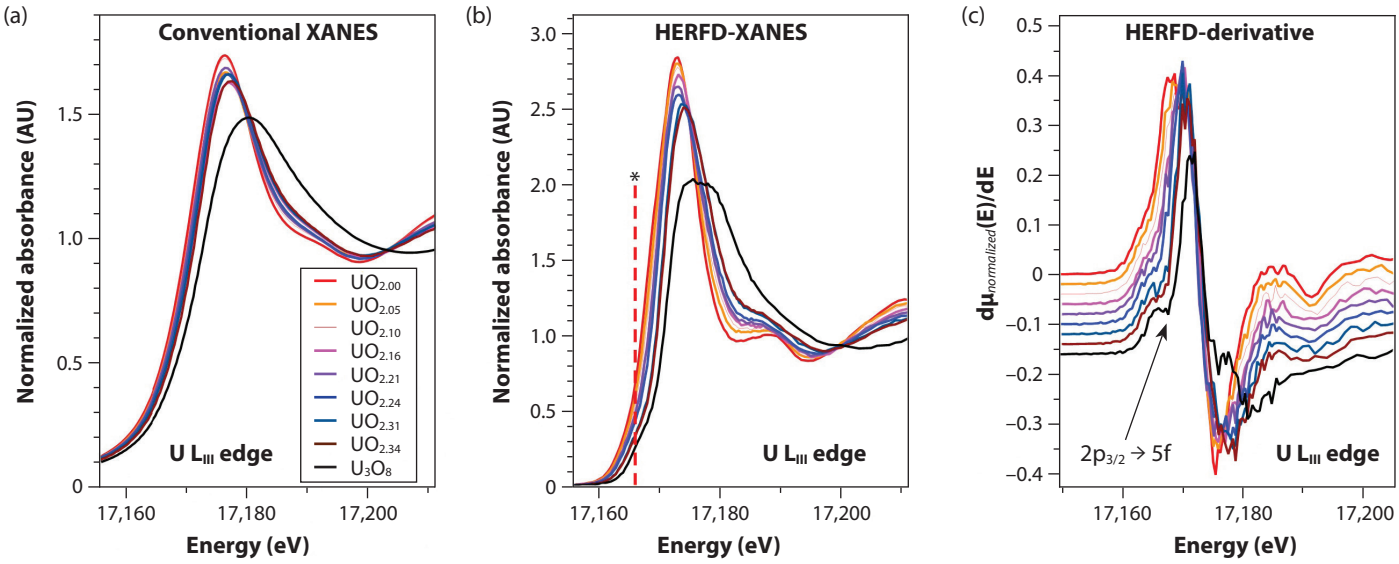

Figure 4. (a) Conventional U L_{III} edge. The spectra of UO_{2+x} show only minute differences (the features are relatively broad due to core-hole lifetime broadening). (b) U L_{III} edge HERFD-XANES using the $L\alpha_1$ emission line. (c) The derivative of the HERFD-XANES spectra. * denotes the increase in the quadrupole pre-edge feature ($2p_{3/2} \rightarrow 5f$).

○ ○ ○

Evaluation of the EXAFS spectra further revealed dramatic effects particularly in the U-O pair correlation, in which a splitting of the U-O interatomic distances was observed (1.94 and 2.35 Å, respectively). These results are expected and typical for hyper-stoichiometric UO_2.

Using the EXAFS results as a basis, we set out to collect HERFD-XANES data to determine the spectrometer resolution needed for calculation of spectral differences and sensitivity to minute changes in UO_{2+x} stoichiometry (Fig. 4). The HERFD-XANES spectra exhibit numerous gradual changes as the stoichiometry shifts from $UO_{2.00}$ to hyper-stoichiometric UO_{2+x}, including:

(i) Increasing intensity of the quadrupole pre-edge feature ($2p_{3/2} \rightarrow 5f$) with increasing values of x, which indicate progressive oxidation of U (highlighted by the tall vertical red line and '*' at ca. 17,166 eV in Fig. 4b). This quadrupole intensity change is diagnostic for U(VI) formation.
(ii) Progressive shifting of the absorbance maximum and main inflection point towards higher energies.
(iii) Changing structure of the peak at ca. 17,186 eV.

These changes indicate the ability to detect subtle chemical signatures. The drastically improved contrast between UO_2 and UO_{2+x} also shows the potential of imaging subtle chemical changes due to the improved variations in intensities, which are currently difficult to disentangle using conventional XANES. Moreover, because of the relatively short acquisition time, this HERFD-XANES method is ideal for coupling with microprobe imaging.

HERFD microprobe imaging: Identifying UO_2 and UO_{2+x} particles

Based on our EXAFS and HERFD results, the HERFD microprobe was designed to meet the minimum spectral resolution threshold to accurately identify UO_{2+x} stoichiometry. To further test our microprobe sensitivity and capabilities, we prepared a sample which had a mixture of UO_2 + U_3O_8 in a soil matrix and UO_2 + $UO_{2.25}$. First, we imaged our sample at 17,250 eV, above the excitation energy of uranium as to locate our uranium particles (Fig. 5). Next, from our bulk HERFD-XANES spectra we calculated the maximum variance between the spectra using principal component analysis. This gave us energies where the spectra differed most. To identify the particles with different oxidation states, we subsequently performed selected excitation energy XAS (SEE-XAS) at the predetermined energies, resulting in seven uranium maps. Using principal component analysis, we identified areas with maximum variance and by using HERFD-XANES point analysis, we could retrieve the stoichiometric value for each component in the map.

Our microprobe showed that we can distinguish between particles with subtly different oxidation states. Furthermore, we were able to locate high-uranium content particles with confidence. Using this approach, we were also able to determine uranium in a complex matrix (soil rich in rubidium). Normally this is difficult as the uranium and rubidium emission lines overlap with each other. Since the resolution of the emission lines from our HERFD spectrometer increased from approximately 250 eV (conventional) to 1.95 eV, we were able to separate those lines and thus were able to accurately identify uranium particles.

These new capabilities provided by the HERFD microprobe represent a large technological jump from conventional imaging using total fluorescence yield or SEM imaging. This is important for forensic analysis of particle sets, in which statistically robust chemical and physical information are of paramount importance. With the development of these capabilities, it will become possible to connect observations to chemical processing steps and implement scientifically rigorous forensic signature sets. Moreover, the development of this technique will speed up the identification of particles from different origins, e.g., naturally-occurring or man-made.

Summary

We have developed a novel HERFD microprobe that can identify particles with subtle molecular variations relevant to nuclear forensic science. This work was motivated by the need to obtain, in a non-destructive manner, nuanced molecular and chemical information at the particle-to-particle level. Our results thus far have shown the potential of XAS and HERFD microprobe imaging to identify detailed chemical signatures of forensic relevant samples in complex systems. These results provide a strong foundation for the continued exploration of nuclear forensic science and will serve as a basis for more complex materials and studies, such as forensic swipes of unknown origin.

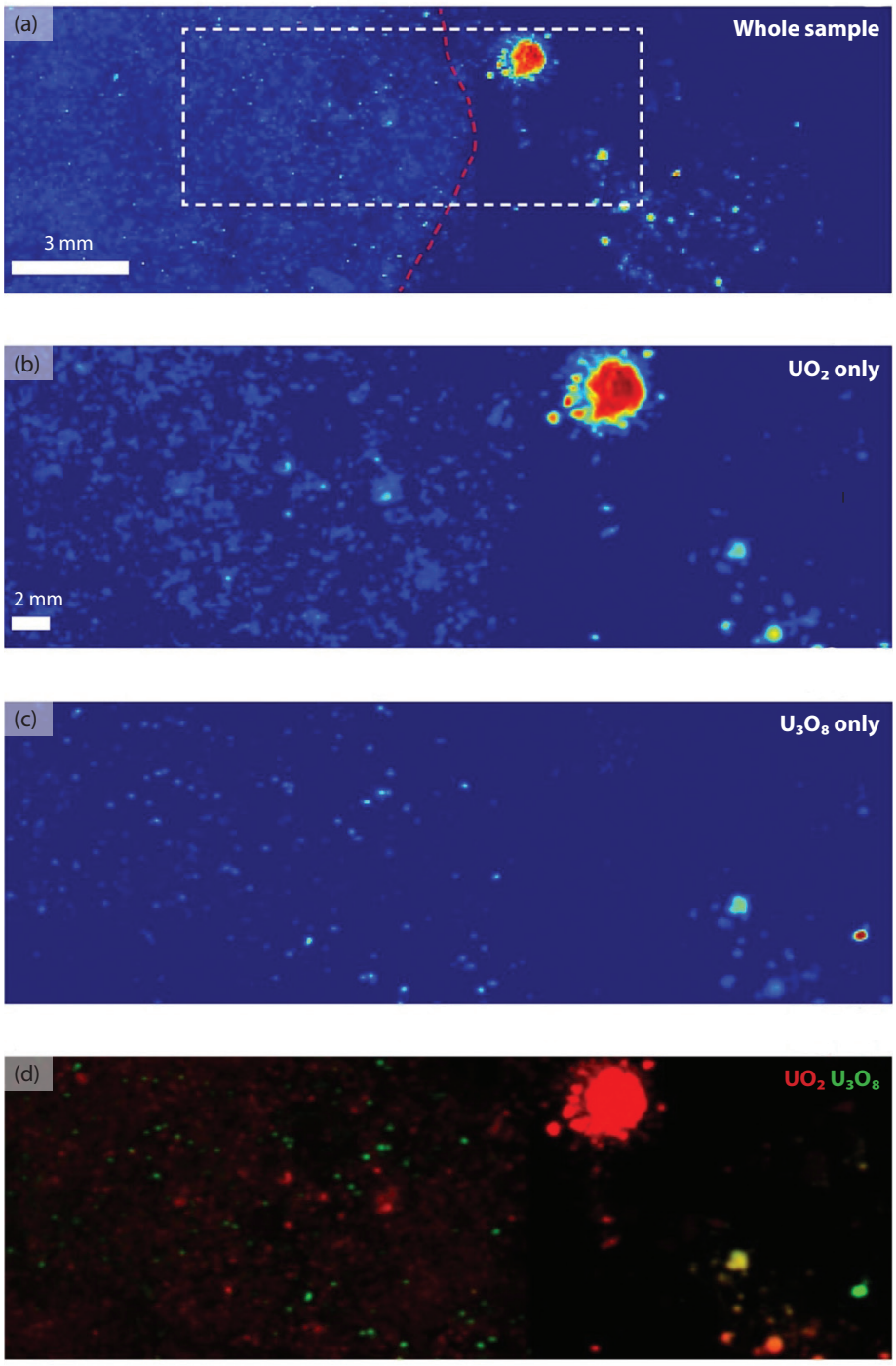

Figure 5. High-energy resolution fluorescence detection (HERFD) imaging data of three uranium oxide compound sample. (a) Initial survey map of whole sample, 33 minute acquisition time. To the left of the red dashed line is the soil matrix, to the right no soil. (b) SEE-XAS fitted data of UO_2. (c) Same for U_3O_8. (d) Bicolor plot of UO_2 (red) and U_3O_8 (green). The area in yellow/orange suggests an area with an oxidation state $UO_{2.25}$. Resolution: 100 µm, dwell time: 25 ms. Data taken from Edwards et al., (2022) "A new µ-high energy resolution fluorescence detection microprobe imaging spectrometer at the Stanford Synchrotron Radiation Lightsource beamline 6-2."

Acknowledgments

This work is a collaborative effort with several other researchers: Sarah M. Hickam, Nicholas P. Edwards, Samuel M. Webb, David L. Clark, Marianne P. Wilkerson, Gregory L. Wagner, Uwe Bergmann all contributed and played vital roles in initiating and continuing this ongoing project. Support for Dr. van Veelen was provided by the U.S. Department of Energy through the LANL/LDRD Program and the G. T. Seaborg Institute. Support was also provided by the NNSA, Defense Nuclear Nonproliferation Research and Development (NNSA DNN R&D) program. Los Alamos National Laboratory is operated by Triad National Security, LLC, for the National Nuclear Security Administration of U.S. Department of Energy (Contract No. 89233218CNA000001). Use of the Stanford Synchrotron Radiation Lightsource, SLAC National Accelerator Laboratory, is supported by the U.S. Department of Energy, Office of Science, Office of Basic Energy Sciences under Contract No. DE-AC02-76SF00515. The SSRL Structural Molecular Biology Program is supported by the DOE Office of Biological and Environmental Research, and by the National Institutes of Health, National Institute of General Medical Sciences (P30GM133894).

Further reading:

1. *A. van Veelen, S.M. Hickam, N.P. Edwards, S.M. Webb, D.L. Clark, M.P. Wilkerson, A.L. Pugmire, J.R. Bargar, "Trace impurities identified as forensic signatures in CMX-5 fuel pellets using X-ray spectroscopic techniques," Anal. Chem., 2022, 94 (19), 7084.*
2. *N.P. Edwards, J.R. Bargar, D. van Campen, A. van Veelen, D. Sokaras, U. Bergmann, S.M. Webb, "A new μ-high energy resolution fluorescence detection microprobe imaging spectrometer at the Stanford Synchrotron Radiation Lightsource beamline 6-2," Rev. Sci. Instrum., 2022, accepted.*
3. *S.D. Conradson, D. Manara, F. Wastin, D.L. Clark, G.H. Lander, L.A. Morales, J. Rebizant, V.V. Rondinella, "Local structure and charge distribution in the UO_2–U_4O_9 system," Inorg. Chem., 2004, 43 (22), 6922.*
4. *A.L. Tamasi, K.S. Boland, K. Czerwinski, J.K. Ellis, S.A. Kozimor, R.L. Martin, A.L. Pugmire, D. Reilly, B.L. Scott, A.D. Sutton, G.L. Wagner, J.R. Walensky, M.P. Wilkerson, "Oxidation and hydration of U3O8 materials following controlled exposure to temperature and humidity," Anal. Chem., 2015, 87 (8), 4210.*
5. *A. van Veelen, J.R. Bargar, G.T.W. Law, G.E. Brown, R.A. Wogelius, "Uranium immobilization and nanofilm formation on magnesium-rich minerals," Environ. Sci. Technol., 2016, 50 (7), 3435.*
6. *O.N. Batuk et al., "Multiscale speciation of U and Pu at Chernobyl, Hanford, Los Alamos, McGuire AFB, Mayak, and Rocky Flats," Environ. Sci. Technol., 2015, 49 (11), 6474.*
7. *M.P. Wilkerson, S.C. Hernandez, W.T. Mullen, A.T. Nelson, A.L. Pugmire, B.L. Scott, E.S. Sooby, A.L. Tamasi, G.L. Wagner, J.R. Walensky, "Hydration of α-UO_3 following storage under controlled conditions of temperature and relative humidity," Dalton Trans., 2020, 49 (30), 10452.*
8. *S.M. Webb, "The MicroAnalysis Toolkit: X-ray fluorescence image processing software," AIP Conf. Proc., 2011, 1365 (1), 196.*
9. *S.X. Cohen, S.M. Webb, P. Gueriau, E. Curis, L. Bertrand, "Robust framework and software implementation for fast speciation mapping," J. Synchrotron Radiat., 2020, 27 (4), 1049.*

Rico Schönemann

Rico Schönemann was a Seaborg Postdoctoral Researcher from August 2019 until March 2022, working under the mentorship of Marcelo Jaime (MPA-MAGLAB). He is currently a postdoctoral researcher in NEN-1 developing instruments based on low temperature detectors. His research interests lie in the study of novel magnetic materials and superconductors at low temperatures and in high magnetic fields.

Uranium Dioxide Sings to the Beat of a Magnetic Hammer

Rico Schönemann
Los Alamos National Laboratory, Los Alamos, New Mexico 87545

Uranium dioxide is one of the most studied actinide materials because of its widespread use as a nuclear fuel in reactors, especially in the high temperature regime at which reactors operate. Interestingly, the first low-temperature measurements on UO_2 were performed under the cloak of the Manhattan Project, revealing a sharp anomaly in the specific heat around 30 K, indicating a phase transition which was suggested to be antiferromagnetic in nature.

Antiferromagnetism was first explained by Louis Néel in 1936. He described it as a type of magnetic order that prefers antiparallel alignment of spins or magnetic moments, as opposed to ferromagnetism in which the alignment is parallel. It took several decades and significant experimental and theoretical efforts to elucidate the exact spin structure of UO_2 and the type of antiferromagnetic order present.

UO_2 crystallizes in the face-centered cubic (fcc) calcium fluoride-type structure, which can be visualized as uranium atoms in a type of cubic lattice with an oxygen cage in the center (Fig. 1a). Above 30 K, UO_2 is a paramagnetic Mott insulator. The antiferromagnetic order of the uranium magnetic moments below 30 K can be described by three wave vectors (3*k*-type) with four spin-sub-lattices pointing along the body diagonals. This 3*k* antiferromagnetic order is accompanied by a Jahn-Teller distortion, a type of structural change which reduces symmetry and lowers the overall energy of the material. This directly impacts its properties as a material: the structural distortion is believed to be a substantial contributing factor to UO_2's extraordinary poor thermal conductivity, which is more than fifty times lower than its isostructural, nonmagnetic analog ThO_2 at low temperatures.

Piezomagnetism in UO_2

The 3*k* magnetic order breaks time-reversal symmetry enabling a phenomenon called piezomagnetism—namely, magnetization that appears when a material is subjected to external pressure (piezo is the Greek word for "push" or pressure). Conversely, linear strain arises when the material is magnetized. This effect happens due to the tilting of the antiferromagnetic sublattices or a change in their relative magnitudes of magnetization. It is analogous to piezoelectricity where applied stress leads to an electric polarization and vice-versa.

Piezomagnetism in UO_2 was discovered in 2017 by magnetostriction measurements in pulsed magnetic fields up to 60 T at 2.5 K, performed at the National High Magnetic Field Laboratory (NHMFL), a pulsed field facility at Los Alamos National Laboratory (LANL). These types of measurements detect a change in sample length when a material is exposed to a magnetic field. Non-destructive resistive pulse magnets were used with a characteristic pulse duration of several tens of milliseconds. The characteristic features observed were linear magnetostriction (a change in sample length) and coercitivity (here, the ability of a material to withstand

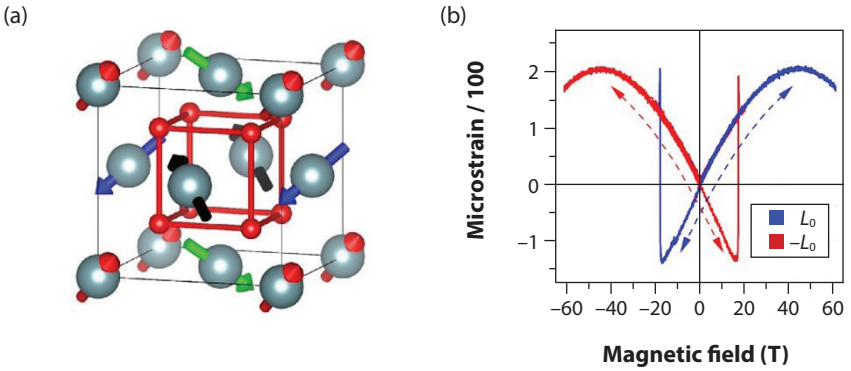

Figure 1. (a) Calcium fluoride crystal structure of UO_2 with the U atoms (grey spheres) forming a cubic (*fcc*) lattice containing the O cage (red bonds/spheres) in the center. The arrows visualize the alignment of magnetic moments forming the 3*k* antiferromagnetic structure with the four magnetic sublattices in different colors. (b) Piezomagnetic butterfly-shaped hysteresis loop of UO_2 measured at 1.7 K in pulsed magnetic fields. The red and blue curves indicate opposite antiferromagnetic ordering vector $\boldsymbol{L_0}$. Sharp transitions are observed at the coercive magnetic fields of ±18 T.

○ ○ ○

a magnetic field without inducing a flip of magnetic domains). These features led to a sharp reorientation of magnetic domains, creating a characteristic butterfly-shaped hysteresis loop (Fig. 1b). The width of the hysteresis extends to ±18 T, making UO_2 the strongest known piezomagnet.

In the paramagnetic state above 30 K, UO_2 does not display piezomagnetism. However, below this temperature in the 3*k* antiferromagnetic state, an additional response emerges from the piezomagnetism which leads to positive magnetostriction at lower fields (Fig. 1b). Also, note that the magnetostriction does not show any sign of suppression of the 3*k* antiferromagnetic order up to 92 T. These results have provided direct evidence for the unusually high energy scale of spin-lattice interactions in UO_2 and motivated studies in magnetic fields in extreme environments beyond 100 T to break the 3*k* order.

Fiber Bragg grating measurements in single-turn coil magnets

To study the high-field magnetostriction and generate magnetic fields significantly above 92 T, we utilized the fiber Bragg grating (FBG) technique (Fig. 2a) in combination with a semi-destructive single-turn coil setup (Fig. 2b,c) at the NHMFL. A peak current of 4 MA flows through the copper coil during the field pulse, causing it to expand and subsequently disintegrate. It might be a general rule that lab explosions are not encouraged at LANL but in this system damage is minor and the sample, cryostat, and probe inside the coil are unharmed. The coil is replaced for each field pulse. The magnetic field peaks at around 150 T after only 3 μs and subsequently shows a damped oscillatory behavior (Fig. 2d). The short pulse duration underlines the need for FBGs as a fast and sensitive dilatometry technique with interrogation rates of several megahertz.

FBGs are types of reflectors built into a short segment of optical fiber (usually less than 10 mm). A portion of the broadband light coupled into the fiber is reflected as a sharp peak, and the wavelength of this peak is sensitive to small changes in the spacing between the gratings. Therefore, it can detect small length changes in any specimen directly glued to it. The sensitivity of the setup used in the single-turn coil magnet is about 10 parts-per-million (ppm). The FBG technique is impervious to

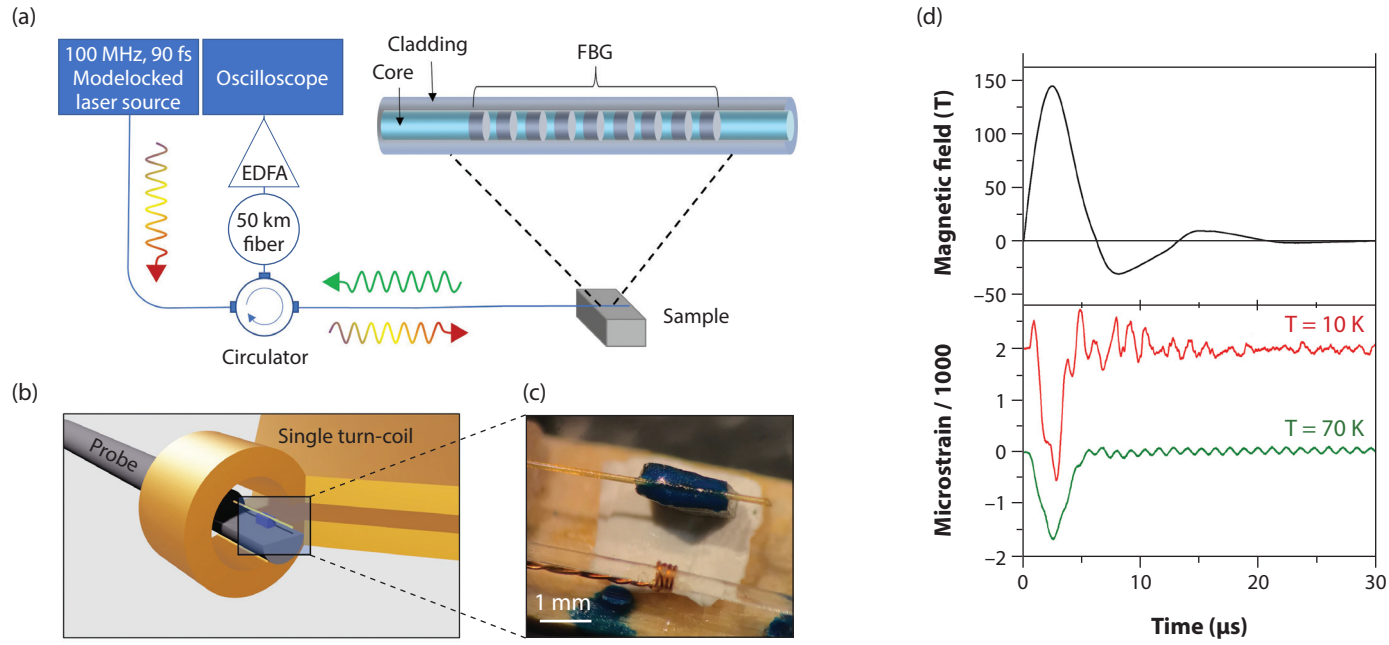

Figure 2. (a) Schematic drawing of the fiber Bragg grating (FBG) setup using a 100 MHz pulsed laser source. The broad-band pulses travel through the optical fiber, and the part of the spectrum reflected by the Bragg grating (FBG) is guided through a 50 km spool of fiber for dispersion before being amplified (erbium doped fiber amplifier, EDFA) and recorded by the oscilloscope. (b) Sketch of the probe and sample within the single-turn-coil (10 mm diameter). (c) Photograph of the sample with the attached optical fiber (*top*) and B-dot coil used for the magnetic field measurement (*bottom*). (d) Profile of the single-turn magnetic field pulse (top) and the relative length change in parts-per-million (microstrain) of a UO_2 sample at 10 K and 70 K as a function of time (*bottom*).

○ ○ ○

electromagnetic interference—this makes it a prime candidate for magnetostriction measurements in single-turn coil experiments, which generate a large amount of electromagnetic noise due to the destruction of the single-turn coil during the magnetic field pulse.

Singing to the beat of a magnetic hammer

The bottom panel of Fig. 2d shows the magnetostriction of UO_2 (i.e., its change in length or microstrain) in magnetic fields up to ~150 T, where the maximum field corresponds to the minimum of the magnetostriction after approximately 2.5 μs. The magnetostriction of the sample is superimposed on strong oscillations or mechanical resonances that are excited almost instantaneously at the beginning of the magnetic field pulse. The extremely large field rate-of-change (about 100 T/μs at the beginning of the pulse) is equivalent to hitting the UO_2 crystal with a "magnetic hammer," exciting a "song" composed of mechanical resonances in the range of several hundred kilohertz.

We can resolve three distinct resonance modes in the temperature range 10–300 K, as seen in the Fourier analysis of the oscillations (Fig. 3a). Thanks to the high quality of the UO_2 single crystal, the characteristic damping timescale is estimated to be around 150 μs. Therefore, we observe little attenuation of the mechanical resonances over the entire measurement time frame. The observed frequencies match those obtained from resonant ultrasound spectroscopy (RUS)—a

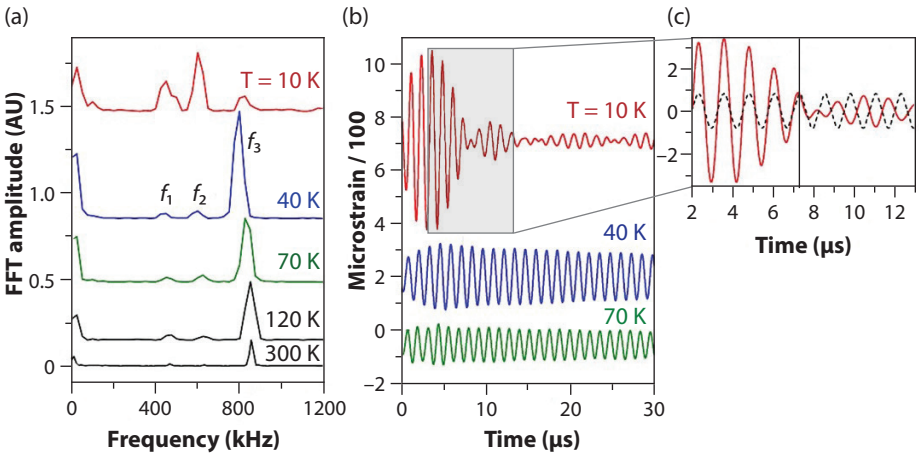

Figure 3. (a) Fast Fourier transforms (FFTs) of the magnetostriction signal at different temperatures, the three dominant resonances are labeled f_1, f_2, and f_3. (b) Oscillatory component of the magnetostriction after bandpass filtering around f_3. (c) A π phase shift is clearly observed at 7 μs.

technique in which resonances are excited as a function of frequency using piezoelectric transducers. In previous measurements in single-turn magnets, similar oscillations were observed but treated as a deleterious effect. By combining our expertise in high magnetic fields, we were able to elucidate magnetic dynamics in UO_2 that have not been explored so far.

Mechanical resonances and piezomagnetic switching

The interesting question is now: How do the mechanical resonances respond to the sudden change of the sample length at ±18 T caused by the piezomagnetic switching of antiferromagnetic domains? (Fig. 1b). As mentioned above, a characteristic of the single-turn coil magnets is a recoil of the magnetic field to approximately –30 T after the main field pulse. Therefore, we would expect an antiferromagnetic domain switch at around 7 μs when the magnetic field falls below –18 T, at which point the sample temperature is below 30 K. Indeed, we observe a substantial change in the mechanical resonances when compared to those seen at temperatures above 30 K.

First, in the data recorded at 10 K, the resonances appear to be significantly damped after approximately 7 μs, particularly the amplitude of the Fourier transform of f_3 (800 kHz), which is smaller compared to f_1 and f_2. This contrasts with the Fourier transforms of the data sets above 30 K, where f_3 is the dominant resonance (Fig. 3a). The attenuation of the signal is shown in Fig. 3b, after isolating the individual resonances and removing the magnetostriction background by way of applying a bandpass filter.

Second, a phase shift of 180° (π radians) is observed in the mechanical resonances at ~7 μs, which is accompanied by the amplitude reduction (attenuation). One can clearly identify the phase shift after a 700–1200 kHz bandpass filter was applied to the data (Fig. 3c). The phase shift coincides with a magnetic field value of approximately –18 T, close to the field value where an abrupt sign change of the antiferromagnetic ordering vector leads to a jump in the lattice distortion characteristic piezomagnetic butterfly (Fig 1b). The origin of the phase shift can be found in the sudden reversal of the antiferromagnetic ordering vector.

Mechanical resonances and FBGs

Mechanical resonances or normal modes are standing waves resulting in periodic deformations in a solid material. The resonant frequencies are determined by the geometry, crystal symmetry, and density of the material as well as its elastic constants. This is leveraged by the resonant ultrasound spectroscopy technique, which measures the resonant spectrum by exciting the sample as a function of frequencies and measure the resonances.

Fiber Bragg gratings (FBGs) can also be used to detect mechanical resonances. These are used as structural health monitors and being considered for embedded sensing applications under extreme conditions due to their robustness under extreme temperatures, high radiation levels, etc. FBGs offer convenient multiplexing capabilities with one fiber containing easily more than ~20 gratings and the ability of modern interrogators to simultaneously probe multiple fibers. As an example, we show here mechanical resonances in an aluminum rod (*below*). A grating was attached to one end of the rod and interrogated with an InGaAs linescan camera with a maximum line rate of ~50 kHz and a strain resolution of 1/10 parts per million (ppm). By calculating the fast Fourier transform (FFT), we can clearly resolve the mechanical resonances up to 5 kHz.

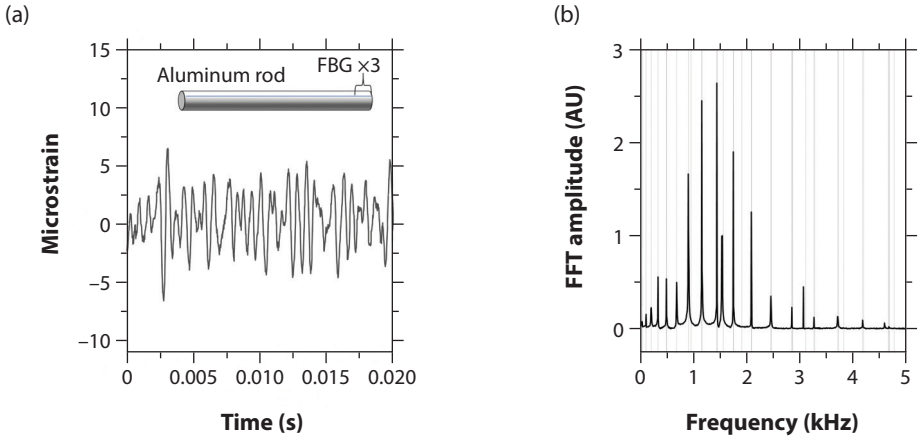

Figure 4. (a) Spatial displacement as a function of time induced on an aluminum rod. (b) Fast Fourier transform (FFT) of the signal shown in (a) and calculated resonances (vertical lines) obtained from a finite element analysis. Calculations were performed by Christopher Mizzi and Luke Beardslee at LANL.

By deriving the equations of motion with respect to the strains, we obtained a driven-oscillator model describing the strain dynamics in UO_2 that led to the phase shift in the mechanical resonances. The attenuation of the resonance can be understood by the dissipative movement of the antiferromagnetic domains throughout the crystal. The sudden movement of domain boundaries at the switching field then leads to the absorption of the elastic energy of the mechanical resonance. Interestingly, only f_3 shows the phase shift and attenuation. The lower frequency resonances f_1 and f_2 seem unaffected. The origin of this behavior could involve the different symmetry of the resonances coupling differently with the antiferromagnetic excitations. Birefringent FBGs that can measure both longitudinal and transversal strains simultaneously could be used in future experiments to learn more about the character of the mechanical resonances and the impact of the piezomagnetic switching. The resonances in UO_2 could also be exploited as a novel class of magnetic field-driven mechanical resonators, given that they are also present in fast pulses up to 20 T.

Summary

We have demonstrated that mechanical resonances can be a valuable tool for detecting otherwise-elusive antiferromagnetic domain flips and other types of crystallographic domain dynamics. Our findings present a novel way to study magnetic dynamics in high fields. They affect the (re-)interpretation of past and future experiments involving compounds with a large magnetoelastic coupling exposed to semi-destructive pulsed magnetic fields and may also have practical implications, e.g., as a method to trigger resonators at faster speeds that are required in single point excitation.

Acknowledgments

This work was conducted as a collaborative effort among several internal and external researchers, including Marcelo Jaime, George Rodriguez, Dwight Rickel, Fedor Balakirev, Ross McDonald, Jordan Evans, Boris Maiorov, Andreas Stier, Myron Salamon (LANL); Charles Paillard, Laurent Bellaiche (University of Arkansas) and Krzysztof Gofryk (Idaho National Lab). Funding and support were provided by the G. T. Seaborg Institute, the National High Magnetic Field Laboratory, which is supported by the National Science Foundation and the state of Florida, the LANL LDRD and the NHMFL UCGP program, the DARPA MATRIX program, the US DOE Early Career Research Program and US DOE BES EFRC "Thermal Energy Transport under Irradiation" (TETI), the US DOE Basic Energy Science program through the project "Science at 100 T" and the LANL Institute for Materials Science.

Further reading:

1. *W.M. Jones, J. Gordon, E.A. Long, "The heat capacities of uranium, uranium trioxide, and uranium dioxide from 15°K to 300°K," J. Chem. Phys. 1952, 20, 695.*
2. *R. Schönemann, G. Rodriguez, D. Rickel, F. Balakirev, R.D. McDonald, J. Evans, B. Maiorov, C. Paillard, L. Bellaiche, A.V. Stier, M.B. Salamon, K. Gofryk, M. Jaime, "Magnetoelastic standing waves induced in UO_2 by microsecond magnetic field pulses," Proc. Natl. Acad. Sci., 2021, 118, e2110555118.*
3. *M. Jaime, A. Saul, M.B. Salamon, V. Zapf, N. Harrison, T. Durakiewicz, J. Lashley, D. Anderson, C. Stanek, J. Smith, K. Gofryk, "Piezomagnetism and magnetoelastic memory in uranium dioxide," Nat. Commun., 2017, 8, 99.*
4. *C.H. Mielke, R.D. McDonald, "Single turn multi-megagauss system at the NHMFL-LOS Alamos to study plutonium", IEEE International Conference on Megagauss Magnetic Field Generation and Related Topics, 2006, 227.*
5. *F.F. Balakirev, S.M. Ennaceur, R.J. Migliori, B. Maiorov, A. Migliori, "Resonant ultrasound spectroscopy: The essential toolbox," Rev. Sci. Instrum., 2019, 90, 121401.*
6. *G. Rodriguez, M. Jaime, F. Balakirev, C.H. Mielke, A. Azad, B. Marshall, B.M. La Lone, B. Henson, L. Smilowitz, "Coherent pulse interrogation system for fiber Bragg grating sensing of strain and pressure in dynamic extremes of materials," Opt. Express, 2015, 23 14219.*
7. *M. Jaime, C.C. Moya, F. Weickert, V. Zapf, F.F. Balakirev, M. Wartenbe, P.F.S. Rosa, J.B. Betts, G. Rodriguez, S.A. Crooker, R. Daou, "Fiber Bragg grating dilatometry in extreme magnetic field and cryogenic conditions," Sensors, 2017, 17, 2572.*

Yogesh Sharma

Yogesh Sharma was a Seaborg Postdoctoral Researcher from Aug. 2019 to Nov. 2021, working under the mentorship of Aiping Chen and Ping Yang. He is currently a Staff Engineer at Applied Materials, Inc. His research interests lie in the development of atomically defined thin film materials for real world applications.

Strain Engineering in Uranium Dioxide Thin Films

Yogesh Sharma

Los Alamos National Laboratory, Los Alamos, New Mexico 87545

Actinide materials have uses in a range of modern commercial and industrial applications: nuclear fuels (uranium-235, plutonium-239), smoke detectors (americium-241), radioisotope thermoelectric generators (plutonium-238), medical isotopes (actinium-225), neutron sources for well logging (americium-241), and numerous other specialized applications. Recent studies have also shown that actinide materials may have applications in quantum computing. Due to strong electronic correlations, actinide materials exhibit wide range of exotic properties but owing to their general scarcity, inherent radioactivity, and synthetic challenges, they represent a poorly understood section of the periodic table. Uranium, however, is readily available and in its depleted form (uranium-238) represents an extremely low radiation risk.

During the past several decades, we have witnessed tremendous breakthroughs in the science of complex oxides enabled by thin-film growth technology. Strain engineering, interface engineering, and defect engineering have been widely used to tune functional properties or create exotic phenomena in thin films. By using the actinide thin film capability established at Los Alamos National Laboratory, we have explored strain engineering of epitaxial (lattice matched) actinide thin films, specifically, uranium dioxide (UO_2).

We have synthesized high quality epitaxial thin films of UO_2 by pulsed laser deposition (PLD) and explored their magnetic properties using a strain engineering approach. The PLD method uses laser pulses focused at a 45° angle on the target (UO_2 in our case) in a high-vacuum chamber and consequently produces a plasma plume—an ionic cloud of constituent atoms (Fig. 1). Depending on the substrate temperature and oxygen pressure inside the chamber, the oxidation state of the uranium metal can be controlled, and hence for a certain growth condition we can create high quality epitaxial thin films on a substrate of our choice.

Strain engineering

Strain engineering in epitaxial thin films has been applied to a variety of non-actinide thin films in the past decade. A lattice mismatch of a few percent between a film and the underlying substrate can produce several GPa of biaxial pressure. This mechanical pressure achieved through epitaxial strain can be used to manipulate the electronic and magnetic ground states in actinide thin films. To apply in-plane tensile and compressive strain, we used the same growth condition to deposit UO_2 films on different substrates by PLD. We selected substrates based on the required strain condition (Fig. 2a). Based on the cubic lattice parameter of 5.471 Å in UO_2, we selected a few available substrates including $YAlO_3$, $LaAlO_3$, $(La,Sr)(Al,Ta)O_3$, and $SrTiO_3$ to tune the epitaxial strain in UO_2.

During the growth of epitaxial heterostructures, the lattice constant difference between the film and the substrate could induce epitaxial biaxial strain. The lattice mismatch (f) can be calculated for these substrates (Fig. 2a). Taking the $SrTiO_3$

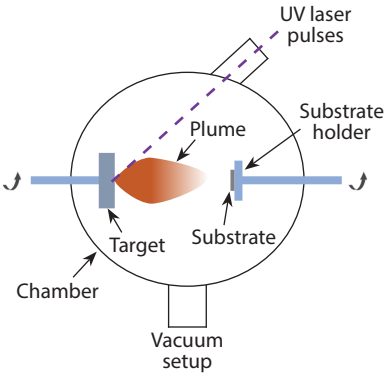

Figure 1. A schematic illustration of pulsed laser deposition process inside a vacuum chamber.

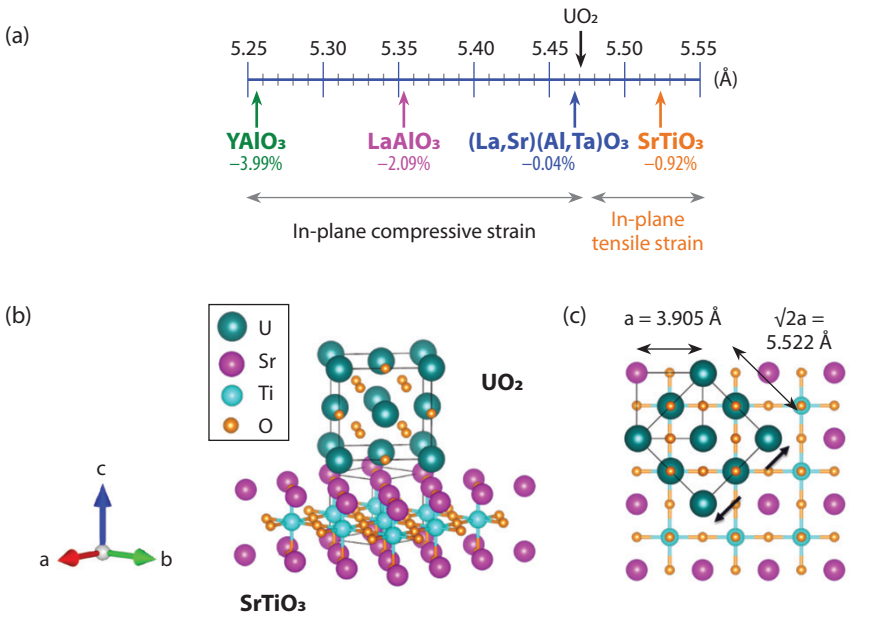

Figure 2. (a) Lattice mismatch between bulk UO_2 and various perovskite substrates. (b) Crystal structure schematic of (001) UO_2 epitaxially grown on (001) $SrTiO_3$, depicting the 45° rotation of the UO_2 unit cell (*above*) with respect to the cubic $SrTiO_3$ lattice (*below*). (c) Epitaxial orientation relationship between the surface mesh of the (001) UO_2 film and underlying (001) $SrTiO_3$ substrate, with one UO_2 unit cell highlighted, which corresponds to a 0.92% lattice mismatch.

○ ○ ○

substrate as an example, the lattice parameter is 3.905 Å for $SrTiO_3$ and 5.471 Å for UO_2. It requires a 45° in-plane rotation to match UO_2 and $SrTiO_3$ substrates (Figs. 2b,c). Through the choice of substrate, we have grown a series of (001)-oriented epitaxial UO_2 films spanning a range of in-plane strain states, yielding nearly (i) compressive strain ($LaAlO_3$, and $YAlO_3$ substrates), (ii) no epitaxial strain ($(La,Sr)(Al,Ta)O_3$ substrate), and (iii) tensile strain ($SrTiO_3$ substrate).

Fig. 3 shows X-ray diffraction longitudinal scans for UO_2 thin films. Only 001 reflections of the UO_2 films are observed in the θ–2θ scans, indicating that all the films are 001 textured and phase pure. Clear thickness fringes are observed around the main diffraction peaks, confirming a uniform thickness and smooth interface for all films. The UO_2 film thickness estimated using these fringes in the diffraction pattern vary from 17–22 nm for the various substrates.

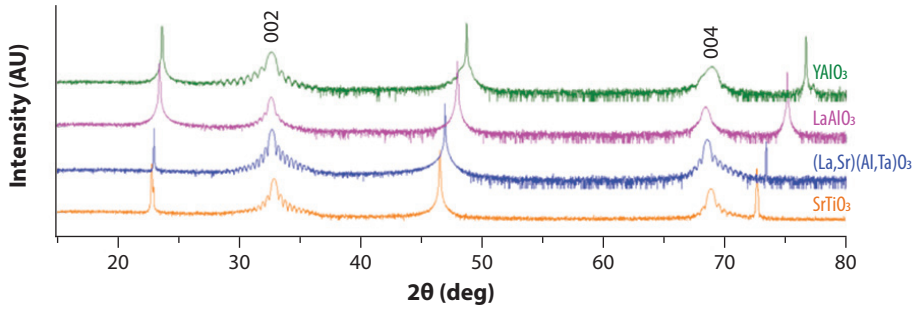

Figure 3. θ–2θ-scans of single-phase (001)-oriented UO_2 films on different substrates.

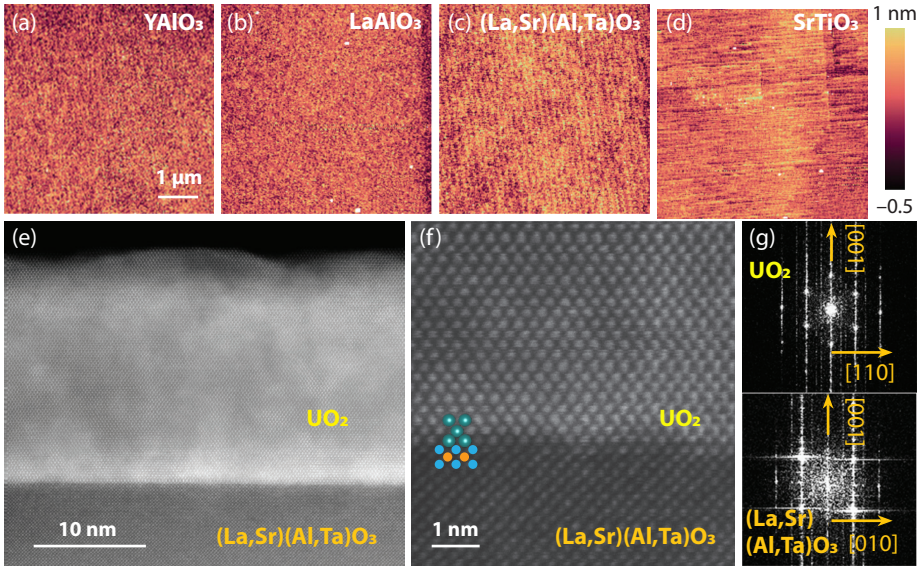

Figure 4. *Top row*: (a-d) Atomic force microscopy images showing atomically smooth surfaces with step terrace structures for films (root mean square surface roughness, measured over the area of 5×5 µm²: 1.4(2), 1.6(2), 1.3(5), and 1.5(4) Å, respectively). *Bottom row:* (e) A cross-sectional STEM image taken along [001] $(La,Sr)(Al,Ta)O_3$ zone axis. (f) STEM image showing an abrupt interface between the UO_2 film and the $(La,Sr)(Al,Ta)O_3$ substrate. (g) Fourier transforms taken from (e) with crystallographic orientations labeled.

o o o

Microstructures

Atomic force microscopy images show that the film surfaces are atomically smooth, presenting steps and terraces (Figs. 4a–d). High-resolution scanning transmission electron microscopy (STEM) was used to characterize the film microstructure and the quality of the film-substrate interface of the UO_2 films on $(La,Sr)(Al,Ta)O_3$ and $YAlO_3$. A sharp interface is seen between the $(La,Sr)(Al,Ta)O_3$ substrate and the film (Fig. 4e) but we see good matching of the atomic lattices at this interface, indicating the high quality epitaxial growth (Fig. 4f). The films are free of misfit dislocations, therefore, there is no evidence that the structures of the films have relaxed, i.e., the films are coherently strained to the substrate.

Magnetism

In bulk, the magnetic moment of UO_2 adopts long range anti-ferromagnetic order below 30.8 K (Néel temperature, T_N). Recent studies have shown the existence of a piezomagnetic effect and hydrostatic pressure-induced ferromagnetic ordering below T_N in bulk UO_2 (see article by Schönemann on p18). These early results from

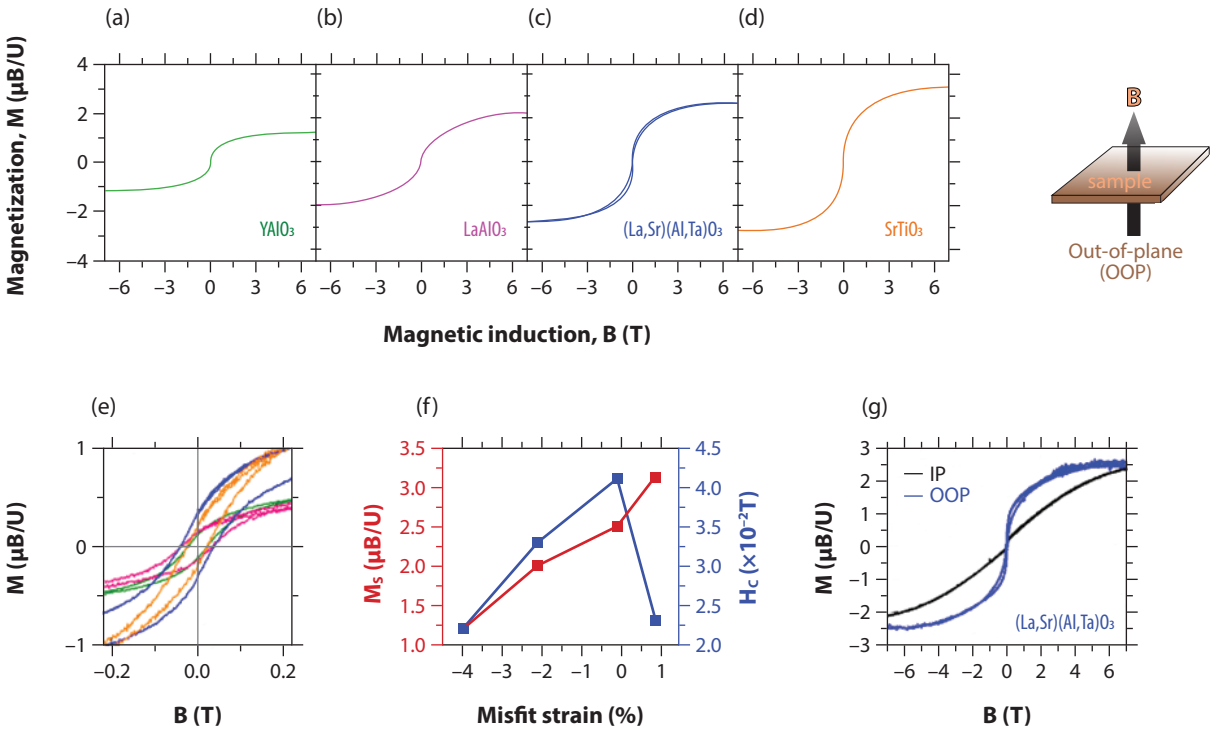

Figure 5. *Top row*: Out-of-plane (OOP) magnetization as a function of applied magnetic field (*M-H*) for UO_2 films grown on (a) $YAlO_3$, (b) $LaAlO_3$, (c) $(La,Sr)(Al,Ta)O_3$, and (d) $SrTiO_3$ substrates at 10 K. *Bottom row*: (e,f) The saturation magnetization and coercive field change while changing the strain from compressive to tensile. (g) Comparison of OOP and in-plane (IP) *M-H* for the UO_2 film on $(La,Sr)(Al,Ta)O_3$ at 10 K. The magnetic easy axis is oriented along the OOP direction in compressive-strained UO_2 on $SrTiO_3$.

○ ○ ○

bulk UO_2 open possibilities for the manipulation of properties using external stimuli such as mechanical strain.

To investigate the effect of biaxial strain (ε) on physical properties, the magnetism of UO_2 films was measured. The magnetization (M) versus magnetic field (H) data were collected by applying the field along the out-of-plane and in-plane directions (Figs. 5a–d show representative out-of-plane $M(H)$ loops taken at 10 K). In comparison with the $M(H)$ loops, the saturation magnetization (M_s) increases as the in-plane strain changes from compressive to tensile. It is evident that the M_s value for a tensile-strained UO_2 film on $SrTiO_3$ (3.22 μ_B/U, ε = –0.93 %) is almost three times larger than the value for a compressive-strained film on $YAlO_3$ (1.08 μ_B/U, ε = 0.15 %). In addition, decreasing compressive strain induces a larger coercivity, although the coercivity decreases for the tensile-strained film (Figs. 5e,f).

These results are consistent with previous work, in which the net magnetization and coercivity of the bulk powdered UO_2 increase by applying hydrostatic pressure. Furthermore, the easy axis of magnetization is found along the out-of-plane direction by comparing the in-plane and out-of-plane $M(H)$ loops for the compressive-strained UO_2 film on $(La,Sr)(Al,Ta)O_3$ (Fig. 5g). These data indicate that the lattice strain has a significant influence on the magnetic properties, with a strong correlation between the lattice and spin orders in UO_2 thin films.

Summary

In summary, we have performed a fundamental study to examine the possibility of using epitaxial strain to tailor the physical properties of UO_2 thin films. High quality epitaxial UO_2 thin films have been grown on various single crystal substrates—X-ray diffraction data demonstrate excellent crystalline quality and smooth interfaces of these strained films. Field-dependent magnetometry shows a ferromagnetic behavior of UO_2 thin films in which the lattice strain strongly affects the net magnetization. The ability to control ferromagnetism with strain and produce a magnetically-uniform insulating thin film should be useful for next-generation magnetic devices. The outcomes of this research will lead to design guidelines towards the functional applications of depleted UO_2 thin films. These results open new approaches to interrogating order parameter coupling in actinide oxides and understanding physical mechanisms.

Acknowledgments

This work is a collaborative effort with several other researchers: Matthew M. Schneider, Pinku Roy, Rico Schönemann, Andrew C. Jones, Marcelo Jaime, Dmitry A. Yarotski, Michael T. Pettes, Ping Yang, and Aiping Chen all contributed and played vital roles in initiating and contributing to this ongoing project. Financial support was provided by the US Department of Energy through the LANL/LDRD program and the Seaborg Institute for the postdoctoral fellowship to Dr. Yogesh Sharma. The work was performed, in part, at the Center for Integrated Nanotechnologies (CINT), an Office of Science User Facility operated for the US Department of Energy Office of Science.

Further reading

1. *H. Idriss, "Surface reactions of uranium oxide powder, thin films and single crystals," Surf. Sci. Rep., 2010, 65, 67.*
2. *J. Mannhar, A. Herrnberger, "The interface is still the device," Nat. Mater., 2012, 11, 91.*
3. *M. Jaime, A. Saul, M. Salamon, V.S. Zapf, N. Harrison, T. Durakiewicz, J.C. Lashley, D.A. Andersson, C.R. Stanek, J.L. Smith, K. Gofryk, "Piezomagnetism and magnetoelastic memory in uranium dioxide," Nat. Commun., 2017, 8, 99.*
4. *A. Chen, Q. Su, H. Han, E. Enriquez, Q. Jia, "Metal oxide nanocomposites: A perspective from strain, defect, and interface," Adv. Mater., 2019, 31, 1803241.*
5. *Y. Sharma, J. Balachandran, C. Sohn, J. T. Krogel, P. Ganesh, L. Collins, A. V. Ievlev, Q. Li, X. Gao, N. Balke, et al., "Nanoscale control of oxygen defects and metal–insulator transition in epitaxial vanadium dioxides," ACS Nano, 2018, 12, 7159.*
6. *E. Enriquez, G. Wang, Y. Sharma, I. Sarpkaya, Q. Wang, D. Chen, N. Winner, X. Guo, J. Dunwoody, J. White, et al., "Structural and optical properties of phase-pure UO_2, α-U_3O_8, and α-UO_3 epitaxial thin films grown by pulsed laser deposition," ACS Appl. Mater. Interfaces, 2020, 12, 35232.*

Tools for Developing Actinium-225 Therapeutics

Kelly E. Aldrich
Los Alamos National Laboratory, Los Alamos, New Mexico 87545

The concept of using radioactive isotopes for medical applications has become commonplace in the last several decades. Each day, tens of thousands of medical procedures across the globe use isotopes such as fluorine-19, technetium-99m, and iodine-123 and -124, coupled with positron emission tomography (PET) and single photon emission computed tomography (SPECT), to image the human body and diagnose diseases. In addition to these diagnostic imaging technologies, the use of targeted radiation can treat diseases. The strategy of infusing radioactive isotopes into the body presents some considerable advantages compared to conventional therapeutics, like those used in chemotherapy. These benefits include potency, reduced off-target side effects, reduced drug resistance, and the potential for personalized medicine. Significant technical challenges must be overcome before these benefits can be realized, however. One major challenge is controlling where an isotope is delivered within the body. Typically, this involves a multicomponent construct that holds the radioisotope with strong chemical bonds (chelator) and delivers it to diseased cells using a biologically active molecule that seeks the specific diseased tissue type (targeting vector). A cartoon representation of this system is shown in Fig. 1, where an antibody represents the targeting vector and representative examples of chelators (ligands that form two or more bonds to a single metal cation) are included.

Even when using an isotope of an element with well-known biochemical behavior, this construct is difficult to achieve. With some of the most promising radioisotopes, including several actinide isotopes, the challenge is even more significant. This is certainly the case for one of the most exciting candidates for targeted alpha therapeutics (TATs), actinium-225 (^{225}Ac). Several of the fundamental nuclear properties of ^{225}Ac make it ideal for clinical application including: a half-life of 9.920(3) days, four successive alpha decays, and the high energy of these alpha emissions (5–6 MeV). However, actinium chemistry is in a state of relative infancy compared to many other elements on the periodic table due to its radioactivity and associated challenges. Aqueous chemistry characterization of actinium is sparse, making it difficult to target/design molecules to bind ^{225}Ac in stable complexes for infusions. The high dose rates, inherent from the short half-life of ^{225}Ac and its daughters, pose significant challenges in handling. The high dose rate also mandates that relatively small quantities are handled at one time, which precludes characterization via macroscopic techniques. Logically, this would lead to characterization by nuclear spectroscopy, where intensity correlates to decay rates rather than mass alone. In the case of ^{225}Ac, however, no convenient γ-emissions characterize the isotope directly and α-spectroscopy gives a convoluted overlapping spectrum in which daughter isotope α-emissions interfere with meaningful analyses. Even if large amounts of this isotope could be safely handled, they are not readily available. ^{225}Ac is in limited supply and typically comes from ^{229}Th decay or is produced directly in high energy accelerators, creating an issue of accessibility.

Kelly Aldrich

Kelly Aldrich joined LANL as a postdoc in May of 2019 and was a Seaborg Postdoctoral Researcher from January 2020 to February 2021. Her postdoctoral research was performed under the mentorship of Stosh Kozimor, Veronika Mocko, and Benjamin Stein. In February 2021, Kelly joined the Actinide Analytical Chemistry group (C-AAC) as a staff scientist where her research efforts are focused on the implementation of new analytical techniques to support the mission scope of the MR&R program at TA-55.

Collectively, these problems make the complex technical challenges that stymie development of ^{225}Ac therapeutics even harder to solve. Our approach to advancing the progress of ^{225}Ac-based alpha therapeutics has focused on solving the problems listed above. Using this strategy, we hope to make R&D tools available to the greater community of actinium researchers to advance the development of this potentially game-changing therapeutic agent.

Actinium-228 as a spectroscopic tool: An underutilized surrogate for clinically relevant isotopes

Natural thorium (^{232}Th, $t_{½}$ = 14 billion years) slowly decays to ^{228}Ac ($t_{½}$ = 6.14(8) hours). The decay of this short-lived actinium isotope to ^{228}Th(β^-) releases unique and high intensity gamma emissions, making it very easy to characterize using routine nuclear spectroscopy. Therefore, ^{228}Ac can be utilized as a surrogate isotope for the clinically significant ^{225}Ac. The decay scheme and γ spectrum of ^{228}Ac are shown in Fig. 3.

The main obstacle to implementing ^{228}Ac as a radiotracer for ^{225}Ac was the issue of harvesting minuscule amounts of ^{228}Ac's direct parent, ^{228}Ra, from bulk ^{232}Th (nanograms of ^{228}Ra are generated in tens of grams of ^{232}Th over many years). Isolating the parent ^{228}Ra creates an ^{228}Ac generator. This generator facilitates repeated ingrowth of the daughter (^{228}Ac) in the parent solution (^{228}Ra). The daughter isotope can then be repeatedly harvested and used for additional experiments by separating the parent and daughter isotopes. This method precludes harvesting the daughter directly using a single-pass method, such as harvesting ^{228}Ac directly from ^{232}Th, which only provides access to the isotope one time.

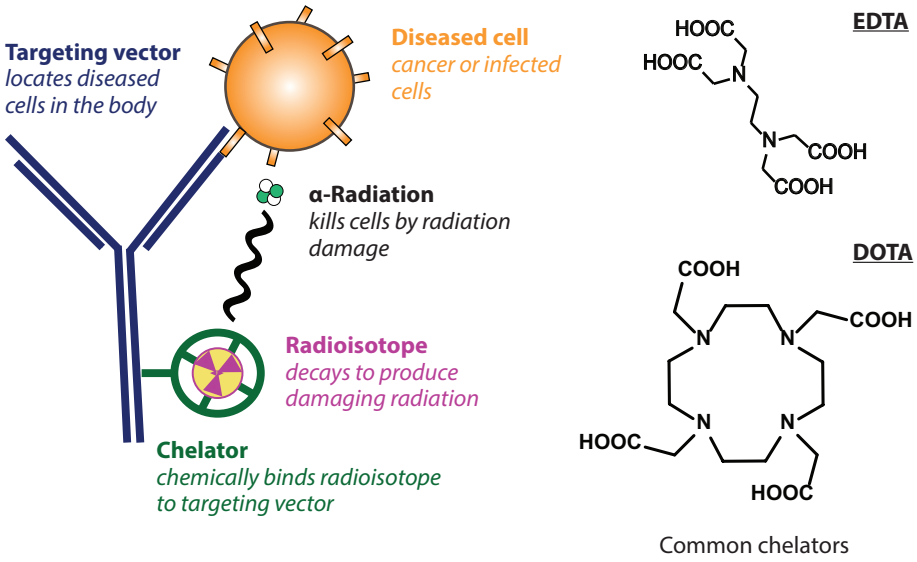

Figure 1. *Left*: Representation of a radioisotope (trefoil) bound to a targeting vector (blue, antibody) by a chelating ligand (green) delivering α-radiation to a diseased cell (orange). The therapeutic agent is the combination of the radioisotope, chelate, and targeting vector. ^{225}Ac makes a promising radioisotope for this application. *Right*: Chemical structures of two of the most widely studied chelating ligands: ethylenediaminetetraacetic acid (EDTA) and 1,4,7,10-tetraazacyclododecane-1,4,7,10-tetraacetic acid (DOTA).

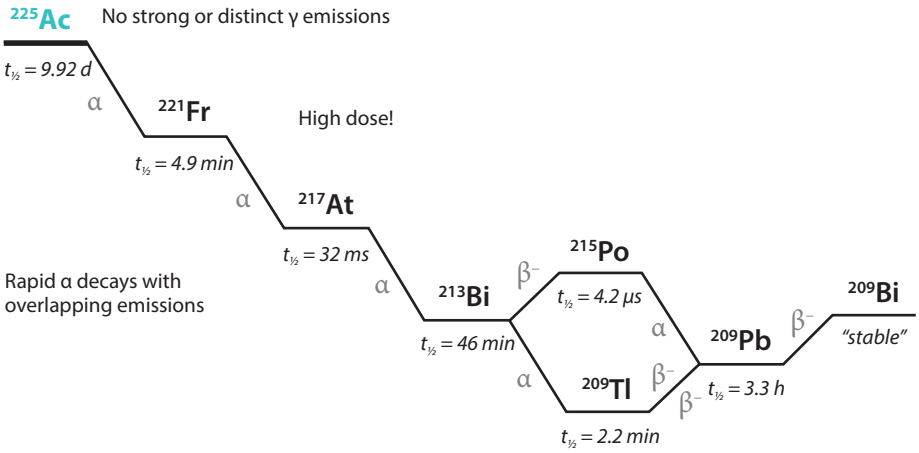

Figure 2. The decay properties of ^{225}Ac are ideal for application in targeted α-therapeutics but restrictive when searching for spectroscopic signatures.

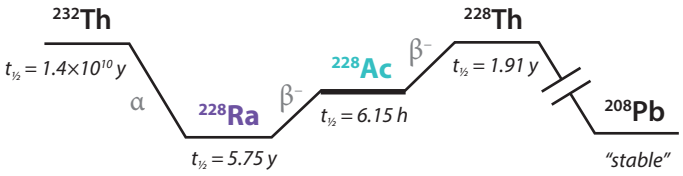

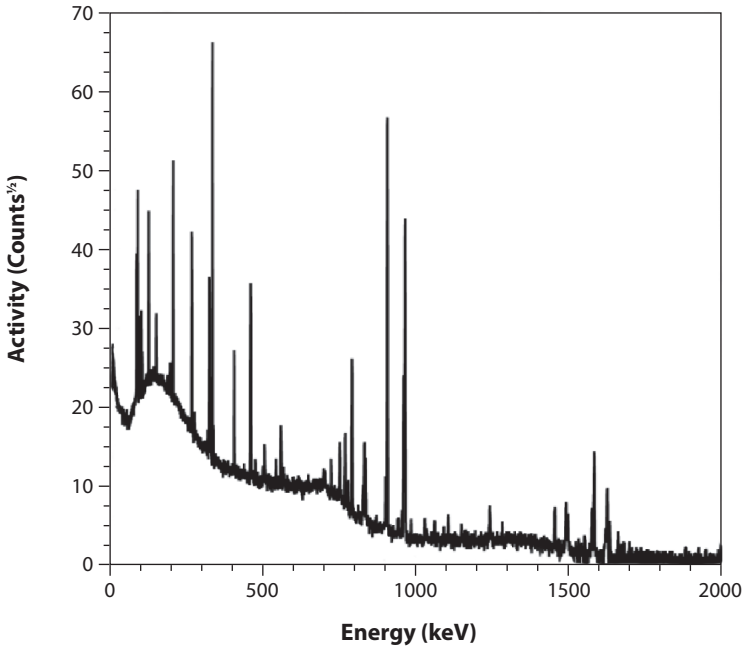

Figure 3. The decay of ^{228}Ac to ^{228}Th results in an abundance of easily detected and quantifiable γ-emissions, as shown in the experimental spectrum of freshly purified ^{228}Ac collected from a ^{228}Ra generator. All emissions shown are characteristic of ^{228}Ac decay.

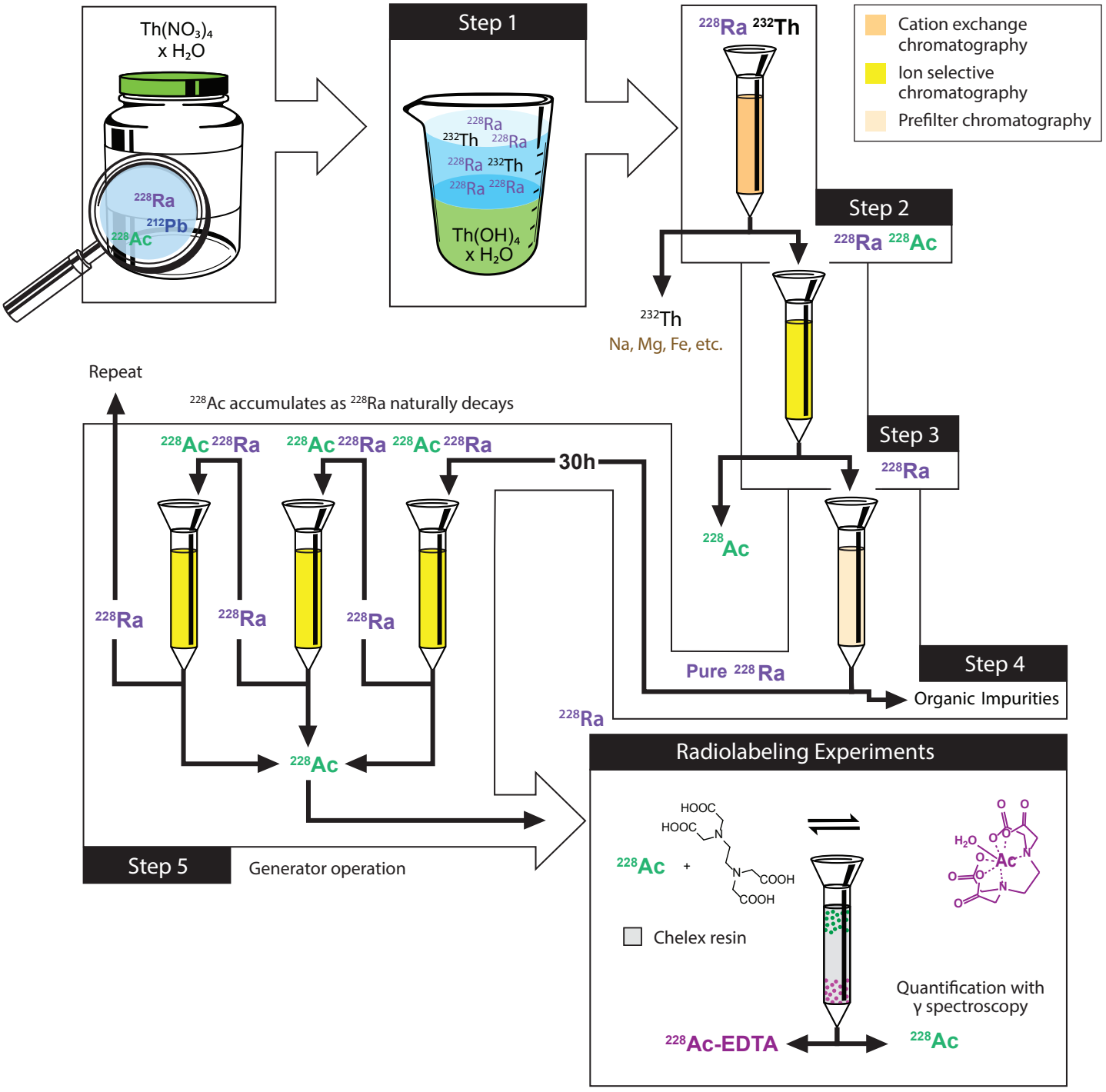

Figure 4. Process overview for creating an ^{228}Ac generator. Thorium-232 salts can be dissolved in water and precipitated from solution by adjusting the pH. The resulting solution, containing ^{228}Ra, a small amount of ^{232}Th, Na^+, and other impurities can be purified by column chromatography in three more steps. The resulting ^{228}Ra solution yields access to ^{228}Ac every 30 hours, giving on-demand access to the spectroscopically friendly ^{228}Ac for further experimentation.

The actinium-228 generator

We developed a four-step procedure by which pure ^{228}Ra can be harvested from aged ^{232}Th (Fig. 4). The ^{228}Ra serves as an on-demand parent source for the desired ^{228}Ac, which grows at a rate proportional to five times the ^{228}Ac daughter's half-life. This means that every 30 hours, the original and maximum amount of ^{228}Ac is replenished in the generator solution from continuous nuclear decay.

The separation process begins with a pH-controlled precipitation (step 1). Next, a series of three resin-based chromatographic separations remove remaining ^{232}Th, minor first-row transition metals, and sodium (step 2); initially present ^{228}Ac (step 3); and organic impurities (step 4). The throughput yield across these four steps provides 83% of the initial ^{228}Ra in radiochemically pure form. The resulting ^{228}Ra stock solution can then be used for on-demand (daily) access to an actinium isotope with the chemical properties of the clinically relevant ^{225}Ac, and the benefits of easy spectroscopic handles with which to identify, quantify, and characterize its behavior directly in solution. The generator procedure is analogous to the chromatographic separation in step 3, which requires about one hour to complete, and provides the targeted ^{228}Ac isotope in 96% yield.

Preliminary experiments have shown that ^{228}Ac harvested from this generator can be used in radiochemical labeling experiments for quantitative analysis of ligand binding. For these experiments, the fast, open-chain chelating ligand EDTA (Figs. 1 and 4) was chosen. Actinium-228 was harvested using a resin-based chromatography technique (as per step 3), providing ~0.7 μCi of ^{228}Ac (98% yield). We applied a standard radiolabeling procedure and achieved repeatable quantification using γ-spectroscopy to identify bound (Ac-EDTA) versus free actinium (Ac^{3+}).

These results provide a workable solution to two of the major problems previously identified as limiting the progress of ^{225}Ac therapeutic chemistry development. First, because ^{228}Ac is the granddaughter of the relatively abundant ^{232}Th isotope, it is far more accessible, both in terms of material and working hazards. This isotope of actinium is accessible to any lab that is equipped to handle natural thorium. Second, the directly detectable γ-emissions of ^{228}Ac facilitate quantification and characterization of its aqueous behavior using routine nuclear spectroscopy.

A systematic ligand family for actinium

With the accessible and readily quantified ^{228}Ac isotope in hand, we were prepared to tackle another challenge facing actinium-based TATs: the challenge of forming stable chelation complexes. By definition, chelators involve multiple bonds to a single metal. Consequently, changing a single component of the structure changes many variables. This makes it difficult to assess the structure-function relationship of a chelating ligand. For medical applications, a good chelator needs to chelate strongly (thermodynamically stable) and rapidly (kinetically favorable). To target these chelate properties, we needed to isolate a single component of the chelating ligand that would change, while the bulk of the ligand would remain unchanged. This would provide a simpler method for identifying trends in bonding related to chelate structure with the goal of answering the question: Which functional groups tend to form strong bonds with actinium?

To choose a constant chelate core, we looked to the literature for a ligand type that has demonstrated effective chelation with large cations. Cyclic chelates with 18-membered rings have shown promising chelation ability towards large cations. The ligand known as Macropa, which is based on a Kryptofix 22 backbone, has been

thoroughly examined as a chelator for $^{225}Ac^{3+}$ by Wilson and coworkers in a series of high impact studies over the last several years (Fig. 5). Using the Kryptofix 22 platform, a two-step reaction process to install different binding arms yields fully functionalized chelates. This simple reaction process is adaptable to a wide variety of binding arms. With this system, changes in the binding strength of the M^{3+}–Kryptofix complexes can be more clearly correlated to the binding arms and their functional groups.

A small series of four Kryptofix 22-based ligands was synthesized following the above methods. As reference points, two important functional groups in the ligand set included the 2-carboxypyridine (Macropa, Ligand-1) and acetic acid (analogous to DOTA, Ligand-4) functional groups as binding arms. A rational design change was also introduced to target improvement on Macropa going from Ligand-1 to Ligand-2 (carboxylates changed to hydroxide groups).

The ligands were examined initially with two stable f-element surrogates of different sizes and Lewis acidities to provide context to the trends ultimately observed when binding studies are expanded to actinium. In this preliminary stage, potentiometry was performed on Ce^{3+} and Gd^{3+} complexes with each ligand to quantify the binding strength of each functional group. The differences in chelate strength with these two lanthanide cations present an interesting picture. Most exciting is the strong bonding achieved with the 2-hydroxypyridine functional group (Ligand 2), especially with the large Ce^{3+} cation. This ligand forms significantly stronger bonds with both metals compared to the next strongest chelators. These results are promising for Ac^{3+} and provide evidence that improvements to existing chelates can be made by tuning their compatibility with f-elements. Additionally, the ordering from weakest to strongest chelation between the two metals was not the same. This suggests that no single cation characteristic is dominant in determining chelate stability. Despite the complexities of predicting chelate stability, these results qualitatively support rational chelate design. An extension of these studies to include actinide cations, and specifically Ac^{3+}, is an ongoing effort. The fundamentals established here with the lanthanide cations provide the basis for these studies to continue in a systematic manner focusing on structure-function relationships.

Summary

The developments outlined here present useful tools for the further advancement of ^{225}Ac-based therapeutic studies. We have established a generator procedure for obtaining on-demand access to the less hazardous and more spectroscopically friendly ^{228}Ac isotope. While the amounts are small, both in terms of mass and absolute activity, a practical set of radiolabeling experiments demonstrated that the ^{228}Ac harvested from the generator is more than sufficient to assess radiolabeling efficiency and facilitate subsequent separation or binding studies. Furthermore, we developed a platform for the systematic evaluation of functional groups on binding stability of chelating ligands, which we tested with f-element surrogates. In combination with the generator-produced ^{228}Ac, this tool could help direct future ligand design for Ac^{3+} chelators.

Acknowledgments

People: Mila Nhu Lam, Laura M. Lilley, Stosh A. Kozimor, Veronika Mocko, Benjamin W. Stein, Sara L. Adelman, Frankie D. White, Cecilia Eiroa Lledo, Trevor Glaros, Ping Yang, Enrique R. Batista. Funding: Seaborg Institute Postdoctoral Fellow Program, DOE, Office of Science, Office of Basic Energy Sciences, the heavy element chemistry program (2020LANLE372), and LANL's LDRD-DR (20180005DR).

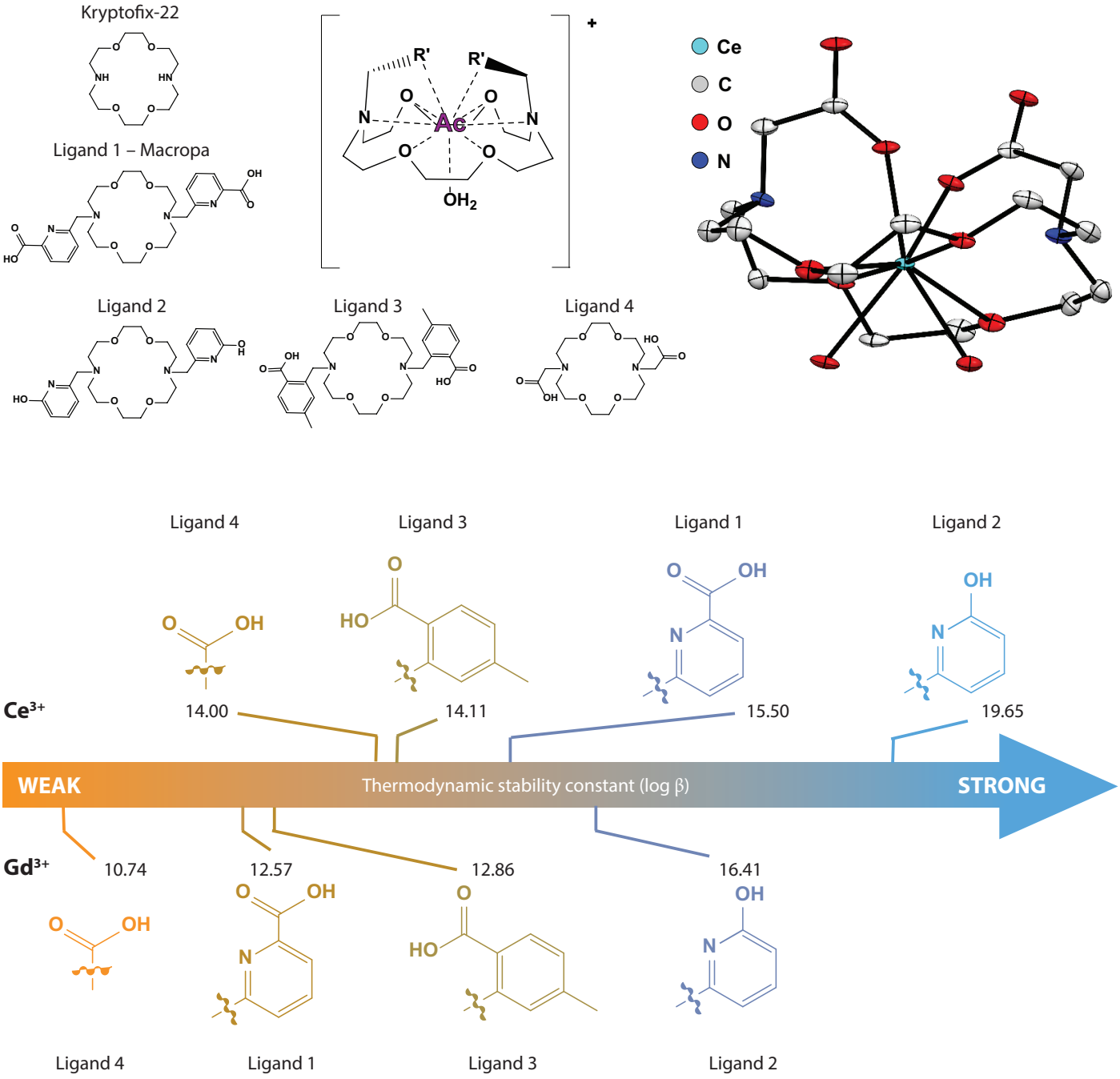

Figure 5. *Top*: Kryptofix® 22-based chelating ligands synthesized for chelation studies targeting actinium. Representative coordination environment is shown between Ac and a generic Kryptofix 22-based ligand. The single crystal X-ray structure of Ligand-3 coordinated to Ce^{3+} is also shown as a representative example of ligand chelation to a metal cation (H atoms and outer-sphere water molecules and counter ions omitted for clarity; thermal ellipsoids shown at 50% probability). *Bottom*: The relative order of chelate strength determined with Ce^{3+} and Gd^{3+}. Left to right, the chelates demonstrated progressively stronger bonding to the metal cation.

Further reading:

1. *National Institute of Biomedical Imaging and Bioengineering, Science Education, Science Topics, Nuclear Medicine, https://www.nibib.nih.gov/science-education/science-topics/nuclear-medicine.*
2. *"Opportunities and approaches for supplying molybdenum-99 and associated medical isotopes to global markets: proceedings of a symposium," National Academies of Sciences, Engineering, and Medicine; Division on Earth and Life Studies; Nuclear and Radiation Studies Board, Washington (DC): National Academies Press (US); 2018 Feb 7. 2, Molybdenum-99/Technetium-99m in Nuclear Medicine. Available from: https://www.ncbi.nlm.nih.gov/books/NBK487238/*
3. *S.M. Ametamey, M. Honer, P.A. Schubiger, "Molecular imaging with PET," Chem. Rev., 2008, 108, 5, 1501.*
4. *T. Ferris, L. Carroll, S. Jenner, E.O. Aboagye, "Use of radioiodine in nuclear medicine—A brief overview," J. Label Compd. Radiopharm., 2021, 64, 92.*
5. *M. Sathekge, F. Bruchertseifer, O. Knoesen, F. Reyneke, I. Lawal, T. Lengana, C. Davis, J. Mahapane, C. Corbett, M. Vorster, A. Morgenstern, "^{225}Ac-PSMA-617 in chemotherapy-naive patients with advanced prostate cancer: a pilot study," Eur. J. Nucl. Med. Mol. Imaging, 2019, 46, 129.*
6. *H. Kulkarni, J. Zhang, T. Langbein, C. Schuchardt, A. Singh, D. Mueller, R. Baum, "Radioligand therapy using combination of Ac-225 and Lu-177 labelled PSMA ligands for progressive end-stage metastatic prostate cancer: effective trade-off between response and toxicity," J. Nucl. Med., 2019, 60, 464.*
7. *S. Satapathy, A. Sood, C.K. Das, B.R. Mittal, "Evolving role of ^{225}Ac-PSMA radioligand therapy in metastatic castration-resistant prostate cancer—a systematic review and meta-analysis," Prostate Cancer Prostatic Dis., 2021, 24, 880 (and references therein).*
8. *National Nuclear Data Center, Brookhaven National Laboratory, Interactive Chart of the Nuclides.*
9. *H. Yang, J.J. Wilson, C. Orvig, Y. Li, D.S. Wilbur, C.F. Ramogida, V. Radchenko, P. Schaffer, "Harnessing alpha-emitting radionuclides for therapy–radiolabeling method review," J. Nucl. Med., 2022, 63 (1) 5.*
10. *K.E. Aldrich, M.N. Lam, C. Eiroa-Lledo, S.A. Kozimor, L.M. Lilley, V. Mocko, B.W. Stein, "Preparation of an actinium-228 generator," Inorg. Chem., 2020, 59, 3200.*
11. *N.A. Thiele, V. Brown, J.M. Kelly, A. Amor-Coarasa, U. Jermilova, S.N. MacMillan, A. Nikolopoulou, S. Ponnala, C.F. Ramogida, A.K.H. Robertson, C. Rodríguez-Rodríguez, P. Schaffer, C. Williams, Jr., J.W. Babich, V. Radchenko, J.J. Wilson, "An eighteen-membered macrocyclic ligand for actinium-225 targeted alpha therapy," Angew. Chem. Int. Ed., 2017, 56, 14712.*

THE GLENN T.
SEABORG
INSTITUTE

Actinide Research Quarterly is published by Los Alamos National Laboratory and is a publication of the Glenn T. Seaborg Institute for Transactinium Science, a part of the National Security Education Center. ARQ (est. 1994) highlights research in actinide science in such areas as process chemistry, metallurgy, surface and separation sciences, atomic and molecular sciences, actinide ceramics and nuclear fuels, characterization, spectroscopy, analysis, and manufacturing technologies.

LA-UR 22-31810

Address correspondence to:
Actinide Research Quarterly
c/o Editor
Mail Stop T-001
Los Alamos National Laboratory
Los Alamos, NM 87545

ARQ can be read online at:
www.lanl.gov/arq

If you have questions, comments, suggestions, or contributions, please contact the ARQ staff at:
arq@lanl.gov

Los Alamos National Laboratory is operated by Triad National Security, LLC, for the National Nuclear Security Administration of U.S. Department of Energy (Contract No. 89233218CNA000001).

Actinide Research Quarterly
Mail Stop T001
Los Alamos National Laboratory
Los Alamos, NM 87545

arq@lanl.gov

Presorted Standard
U.S. Postage Paid
Albuquerque, NM
Permit No. 532

Los Alamos NATIONAL LABORATORY

THE GLENN T. SEABORG INSTITUTE

NNSA